



**HAL**  
open science

# Velocity, stress and concentration fields revealed by micro-PIV and SAXS within concentration polarization layers during cross-flow ultrafiltration of colloidal Laponite clay suspensions

Candice Rey, Nicolas Hengl, Stéphane Baup, Mohamed Karrouch, Alain Dufresne, Henda Djeridi, Rajeev Dattani, Frédéric Pignon

## ► To cite this version:

Candice Rey, Nicolas Hengl, Stéphane Baup, Mohamed Karrouch, Alain Dufresne, et al.. Velocity, stress and concentration fields revealed by micro-PIV and SAXS within concentration polarization layers during cross-flow ultrafiltration of colloidal Laponite clay suspensions. *Journal of Membrane Science*, 2019, 578, pp.69-84. 10.1016/j.memsci.2019.02.019 . hal-02048008

HAL Id: hal-02048008

<https://hal.science/hal-02048008>

Submitted on 22 Oct 2021

**HAL** is a multi-disciplinary open access archive for the deposit and dissemination of scientific research documents, whether they are published or not. The documents may come from teaching and research institutions in France or abroad, or from public or private research centers.

L'archive ouverte pluridisciplinaire **HAL**, est destinée au dépôt et à la diffusion de documents scientifiques de niveau recherche, publiés ou non, émanant des établissements d'enseignement et de recherche français ou étrangers, des laboratoires publics ou privés.



Distributed under a Creative Commons Attribution - NonCommercial 4.0 International License

1     **Velocity, stress and concentration fields revealed by micro-PIV and SAXS**  
2     **within concentration polarization layers during cross-flow ultrafiltration of**  
3             **colloidal Laponite clay suspensions.**

4  
5     C. Rey<sup>1,2</sup>, N. Hengl<sup>1\*</sup>, S. Baup<sup>1</sup>, M. Karrouch<sup>1</sup>, A. Dufresne<sup>2</sup>, H. Djeridi<sup>3</sup>, R. Dattani<sup>4</sup>, F. Pignon<sup>1\*</sup>

6  
7             <sup>1</sup>Univ. Grenoble Alpes, CNRS, Grenoble INP\*, LRP, 38000 Grenoble, France

8             <sup>2</sup>Univ. Grenoble Alpes, CNRS, Grenoble INP\*, LGP2, 38000 Grenoble, France

9             <sup>3</sup>Univ. Grenoble Alpes, CNRS, Grenoble INP\*, LEGI, 38000 Grenoble, France

10             (\* Institute of Engineering Univ. Grenoble Alpes)

11             <sup>4</sup>ESRF, The European Synchrotron, CS 40220, 38043 Grenoble Cedex 9, France

12  
13     **Abstract**

14     This study focuses on bringing a better understanding of the mechanisms involved in the formation of  
15     the concentration polarization and fouling phenomena during the cross-flow ultrafiltration process of  
16     colloidal Laponite clay suspensions. New cross-flow ultrafiltration cells were designed to perform  
17     firstly time resolved *in-situ* small angle X-ray scattering (SAXS) and secondly time resolved *in-situ*  
18     micro particle image velocimetry (micro-PIV) at the vicinity of the membrane surface during the  
19     filtration. These two methods have allowed to access to the concentration profiles and the velocity  
20     field as a function of the distance  $z$  from the membrane surface with respectively 20  $\mu\text{m}$  and 30  $\mu\text{m}$   
21     accuracy, within the concentration polarization layers. The results obtained show an increase of the  
22     volume fraction related to a decrease of the velocity within the layers formed during the process. The  
23     correlation of these results with the rheological behavior of the suspensions permitted to access to the  
24     calculated stress field within the concentrated layers during the cross-flow ultrafiltration process.  
25     Three different regions near the membrane surface have been emphasized with different shear  
26     stress/shear rate behaviors. The important role of the rheological behavior and inter particle interaction  
27     in the dynamic evolution in space and time of the accumulated layers has been highlighted.

28     \*Corresponding authors at: CNRS, Univ. Grenoble Alpes, LRP, F-38000 Grenoble, France

29     Email addresses: frederic.pignon@univ-grenoble-alpes.fr (F. Pignon); nicolas.hengl@univ-grenoble-  
30     alpes.fr (N. Hengl)

31 **Key words:** *cross-flow ultrafiltration, micro-PIV, velocity field, shear stress, concentration*  
32 *polarization layer*

33

## 34 **1. INTRODUCTION**

35 Membrane separation processes are commonly used in several industrial applications, like bio and  
36 agro industries, waste and water treatments, and more recently biorefinery. Ultrafiltration process  
37 permits concentrating or separating colloidal suspensions, for several applications like food,  
38 pharmaceuticals, cosmetics, chemical, nuclear, and automotive industries among others.

39 Although it presents numerous advantages, the stability of the crossflow ultrafiltration process is  
40 governed by the increase of particle concentration at the membrane surface due to simultaneous effect  
41 of the shear involved by the flow and the pressure forces generated by the transmembrane pressure  
42 (TMP). These two external forces in competition with internal colloidal forces lead to the formation of  
43 two phenomena named concentration polarization and fouling of the membrane, which decrease the  
44 filtration performance [1-5]. [This phenomenon of concentration polarization layers was evidenced in](#)  
45 [ultrafiltration processes as well as in others processes like microfiltration processes \[6\] reverse](#)  
46 [osmosis \[7\] as well as direct contact membrane distillation systems \[8\] used for treating very high](#)  
47 [salinity produced water. In ultrafiltration processes,](#) these concentrated layers have a thickness of tens  
48 to few hundreds micrometers depending on the filtration conditions and the inter-particles interaction  
49 within the filtrated suspension and can generate a decrease of the permeate flux of 50 %. Thus, it is of  
50 primary interest to characterize the particles organization and interactions within these accumulated  
51 layers (hundreds of micrometers thick) and to understand the mechanisms involved in the  
52 concentration phenomena during the ultrafiltration process.

53 [Several previous works have investigated the formation of the concentrated layer during this filtration](#)  
54 [process and showed an increase of the concentration near the membrane surface in relation with the](#)  
55 [decrease of the permeation flux \[9-11\]. Some experimental investigations have probed the deposit](#)  
56 [formation at different length scales by means of different approaches. Specific \*in-situ\* monitoring](#)  
57 [techniques have been developed and have been reviewed by Chen et al. \[12\]. To understand the](#)  
58 [mechanisms of cake formation and fouling mechanisms, some techniques are more dedicated to](#)  
59 [characterize the particle deposition, thickness of deposit and cake layer formation. In a general way,](#)  
60 [the whole of the characterization techniques used can be separated in two domains of length scales](#)  
61 [probed: at micrometric and nanometric length scales.](#)

62 [Firstly, at micrometric length scales some optical non invasive methods like optical, confocal or](#)  
63 [fluorescence microscopy, have been implemented by means of direct observation through or above the](#)

64 membrane to characterize the organization of the deposited particles [13-15]. The increase of the  
65 concentration inside the concentration polarization layers has been optically investigated by  
66 holographic interferometry [16] during a microfiltration process. This optical method has allowed  
67 quantifying the increase of concentration in the vicinity of the microfiltration membrane before  
68 reaching a “pseudo steady state” after 20 minutes of filtration. Others techniques like, nuclear  
69 magnetic resonance (NMR) have been put in operation to investigate the phenomena during the  
70 filtration of colloidal silica suspensions using a single tubular microfiltration membrane [17]. The  
71 authors are able to reach the concentration polarization profile in the filtration device and show that  
72 the axial component of the flow is driven by the shear induced cross-flow filtration. Another example  
73 of concentration polarization investigation is reported by Donogh et al. [18] using two different non-  
74 intrusive techniques for different filtration processes. The authors observed a similar phenomenon for  
75 different pore sizes and a good match between literature value and measured value concerning the  
76 thickness of the concentration polarization layer in each processes for radioactively labelled protein  
77 suspensions. More recently, a new optical method using a laser sheet has been developed and  
78 validated to characterize *in-situ* the cake formation in a narrow channel, to obtain the mechanisms of  
79 cake growth and better understand the relationship between deposit structure and process performance  
80 [19-21]. New microfluidic devices in poly-dimethyl siloxane have also been developed for dead-end  
81 and cross-flow filtration, which allow direct observation of clogging dynamics in microchannels (20  
82  $\mu\text{m}$ ) wide by micrometric particles (5  $\mu\text{m}$ ) [22-23]. The results allow distinguishing different clogging  
83 behaviors according to filtration conditions and considering the different interaction (particle - particle  
84 and particle - wall) colloidal interactions. At larger length scales, direct optical observation of the  
85 surface of a single hollow fiber membrane have been performed during cross-flow filtration of  
86 monodisperse polymer model particles with varying surface charge densities [24]. Some recent  
87 measurement by fluid dynamic gauging have investigate *in-situ* the thickness and cohesive strength of  
88 cake fouling layers formed during cross-flow microfiltration of a softwood kraft lignin model system  
89 [25].

90

91 Secondly, at nanometer length scales, some *ex-situ* or *in-situ* scattering techniques, like small-angle  
92 neutron scattering (SANS) as well as small angle x-ray scattering (SAXS) have been used to probe the  
93 structural organization of colloids during the filtration processes. Thanks to the development of a  
94 filtration cell dedicated to neutron scattering, *in-situ* SANS measurements have allowed monitoring  
95 the *in-situ* development of the fouling layer inside the membrane pores [26]. The mechanisms of cake  
96 collapse in dead-end filtration have been studied and elucidated by filtration of aqueous dispersions of  
97 latex particles aggregated by  $\text{CaCl}_2$ . *Ex-situ* SANS experiments on filtered cakes in different pressure  
98 conditions have allowed to show that the mechanisms of cake collapse are made of very small relative

99 motions of the particles, which leave the local coordination of the latex particles unchanged but allow  
100 large voids to be reduced [27]. In the same manner SANS and transmission electron microscopy have  
101 been linked to determine the process by which the particles move and reorganize during cake collapse  
102 [28]. Combination of static light scattering , SANS and local birefringence techniques have been used  
103 to quantify the inner structure, structural orientation and organization of deposited colloid fouling  
104 layers on the membrane surface during dead-end filtration of Laponite clay dispersions [29]. Some  
105 developed dead-end filtration cells, simultaneously applying a transmembrane pressure and a magnetic  
106 field have allowed to simultaneously characterize by SAXS, the structure of particle deposit during  
107 ultrafiltration, manipulate the particle orientations and enhance the filtration performance [30]. On the  
108 same principle custom made ultrafiltration dead-end cells have allowed get access to the *in-situ*  
109 structural organization of casein micelle suspensions by SAXS and the corresponding spatial and  
110 temporal *in situ* concentration profile evolution during dead-end filtration [31-32].

111 On the bases of these dead-end ultrafiltration cells, dedicated to SAXS measurements, some others  
112 cross-flow ultrafiltration cells and ultrasound coupled cross-flow ultrafiltration cells have been  
113 designed to perform *in-situ* SAXS. Thanks to these cells, concentration profiles and structural  
114 organizations have been explored as a function of the distance  $z$  from the membrane surface, for  
115 different colloidal systems, in different cross-flow filtration / ultrasound conditions [33-36].

116 Apart from these structural characterization of the deposited particles near the membrane surface,  
117 some measurements or numerical modelling have been done to access to the velocity fields in  
118 filtration processes [37-39]. Nevertheless some important information like the velocity field near and  
119 inside the concentrated layer formed during crossflow ultrafiltration and the corresponding local shear  
120 stresses are still missing to overcome the phenomena involved during the filtration. This knowledge is  
121 necessary to develop the theoretical models and improve the understanding of stability of the  
122 ultrafiltration process and the related mechanisms responsible of the concentration polarization  
123 phenomena. The objective of this study is to use *in-situ* scattering techniques and develop micro-PIV  
124 investigations to get access to concentration profiles, velocity fields and deduce the corresponding  
125 calculated shear stresses inside the accumulated layer during membrane separation processes.

126 New cross-flow ultrafiltration cells were designed to perform firstly time resolved *in-situ* small angle  
127 X-ray scattering (SAXS) and secondly time resolved *in-situ* micro particle image velocimetry (micro-  
128 PIV) at the vicinity of the membrane surface during the filtration. The SAXS measurement performed  
129 *in-situ* during ultrafiltration of Laponite clay suspensions allowed characterizing the structural  
130 organization at the nanometer length scales and concentration profiles measured as a function of the  
131 distance  $z$  from the membrane surface with 20  $\mu\text{m}$  accuracy. These structural and concentration  
132 information's have been linked to the permeate flux, cross-flow and transmembrane pressure registered  
133 simultaneously. In the same manner, the micro-PIV measurements have allowed to establish the

134 velocity field evolutions and corresponding shear rate as a function of the distance  $z$  with  $30\ \mu\text{m}$   
135 accuracy, within the concentration polarization layers and during filtration time. These concentration  
136 and shear rate evolutions in space and time, were then correlated to the rheological behavior of the  
137 suspensions, in order to calculate the corresponding stress field evolutions within the concentration  
138 polarization and fouling layer during the cross-flow ultrafiltration process.

139

## 140 **2. MATERIALS AND METHODS**

### 141 **2.1 Sample preparation**

142 The clay used in this study was Laponite XLG which comes from Laporte Industries. It is a synthetic  
143 disk-shaped Laponite  $30\ \text{nm}$  in diameter and  $1\ \text{nm}$  in thickness. The particles have a density of  $2.53\ \text{g}\cdot\text{cm}^{-3}$ .  
144 The suspension was prepared by mixing the Laponite powder with demineralized water at  $20\ ^\circ\text{C}$   
145 with a fixed ionic strength of  $10^{-3}\ \text{M}$  NaCl and  $\text{pH} = 10$ , following the protocol used by Jin *et al.*  
146 [34]. Suspensions to be filtered were prepared at a volume fraction of  $1\ \text{vol}\%$ . The suspension aged in  
147 closed bottle during 12 to 26 days before the filtration experiments. As shown before the structure and  
148 the rheological behavior evolves during the aging time and the value of the yield stress increases for  
149 increasing aging time [33, 40-43]. Changes were observed in the viscoelastic properties and structural  
150 characteristics of the gels over time. This is due, in part, to the osmotic swelling caused by repulsion  
151 between the double layers and also to the progressive organization of the particles into fractal  
152 aggregates over larger length scales as already studied in details [40]. Ruzicka and co-workers [42] are  
153 able to identify the presence of two distinct arrested states. While repulsion is felt almost immediately  
154 after samples are prepared, attraction, due to its anisotropic nature and to the presence of an effective  
155 repulsive barrier, develops on a much longer time scale. More recently [43] this aging dynamics was  
156 studied as a function of solid content, salt, concentration and pH, and discuss in term of the edge to  
157 face or face to face contact between the particles. Consequently, to pass over this aging phenomena,  
158 the time  $t_p$  that has elapsed between the end of the preparation and the different structural or filtration  
159 investigations will always be indicated in the following. For the different kinds of measurements  
160 (rheometric behavior, cross-flow ultrafiltration) the results will be compared at the same  $t_p$  time.

161 The interaction can be controlled by the addition of a peptizer which reduces the positive charges and  
162 change the global charge of the particles to be repulsive. The peptizer used in the present study is the  
163 tetrasodium diphosphate  $\text{Na}_4\text{P}_2\text{O}_7$  (tspp) and has a molecular weight of  $446\ \text{g}\cdot\text{mol}^{-1}$ . The effect of the  
164 peptizer on the rheological behavior and the structure has already been studied in previous works [34,  
165 40]. The reduction of the interaction leads to a change in the rheological properties from yield stress  
166 fluids to shear thinning fluids behavior with the addition of peptizer. Several suspensions were  
167 prepared for the rheometric measurements denoted  $L(i)\text{-Cp}(0\ \text{or}\ 6)$ , with  $i$  corresponding to the volume

168 fraction content, and 0 or 6 corresponding to the  $C_p$  concentration in peptizer equal respectively to 0%  
169 or 6% of the mass fraction of dry clay.

## 170 2.2 Rheometric measurements

171 Rheometric measurements were carried out using a shear rate controlled rheometer (ARG2, TA  
172 Instrument) with a cone – plate geometry of 49 mm in diameter and with an angle of  $4^{\circ}21'$  in the same  
173 conditions as [34]. In order to avoid interfacial effect, the surface of the plate geometry has been  
174 covered with sand paper with a roughness of 200  $\mu\text{m}$ . Measurements were performed at a fixed  
175 temperature of  $25 \pm 1$  °C. An evaporation proof system has been added on the top of the geometry to  
176 ensure the saturation of the atmosphere of the sample.

## 177 2.3 SAXS cross-flow filtration: cell and filtration procedure

178 A SAXS coupled to cross-flow filtration cell was designed to measure *in-situ* concentration profiles  
179 and structural organization of the colloidal suspensions during the time of filtration (**Fig. 1 a, b**). This  
180 information is obtained as a function of the distance  $z$  from the membrane surface. The cell was made  
181 of transparent polycarbonate and the membrane was a flat sheet of polyethersulfone of (100 x 4) mm  
182 (100 kD, Pleyade, Orelis environnement). The filtration cell is composed of two polycarbonate pieces  
183 with a retentate channel for the upper part and the permeate channel for the lower part. The retentate  
184 channel was 100 mm long in  $x$  cross-flow flow direction and the flow section was 7.4 mm  $z$  high for 4  
185 mm  $y$  large. Three windows of observation were positioned at the entrance, the middle and the outlet  
186 of the cell at 43 mm of each other. These windows had a dimension of (3 x 5.5 x 0.3) mm,  
187 respectively, in width, height and thickness. The permeate channel was 100 mm long in  $x$  cross-flow  
188 flow direction and the flow section was 10 mm  $z$  high for 4 mm  $y$  large. The membrane is strengthen  
189 between these two upper and lower parts of the cell. The  $z_c = 0$  position of the filtration cell,  
190 correspond to the edge of the membrane in contact with the permeate lower part of the filtration cell.  
191 During the filtration, the feed suspension was pumped (Mono pump LF series, Axflow) from a high  
192 pressure tank (Millipore). Pressure was applied to the rig via purified compressed air and the retentate  
193 pressure  $P$  was measured at the inlet and outlet of the cell with a pressure gauge (FP 110 FGP Sensors  
194 & Instrument). Cross flow flux was continuously measured (Optiflux 6300C flowmeter, Krohne). The  
195 permeate flux was recovered and weighed during the time with an accuracy of 0.001 g every 5 s  
196 (balance Precisa 400 M). During the filtration the temperature was monitored by a cryo thermostat  
197 (Thermo & Scientific SC, 150 A25, HAAKE) and fixed at 25 °C. Filtration procedure with several  
198 steps was performed for the Laponite suspensions as described by **table 1** for each system. To  
199 emphasize the phenomenon about the formation of the concentration layer during the ultrafiltration  
200 process, only the last filtration step at  $0.06 \text{ L}\cdot\text{min}^{-1}$  concerning these two kinds of suspension will be  
201 presented in detail.

202

### 2.3.1 *In-situ* SAXS cross-flow filtration: conditions and analysis

203 SAXS experiments were performed at the European Synchrotron Radiation Facility (ESRF, Grenoble,  
204 France), at the ID02 TRUSAXS beamline. The incident X rays beam had a wavelength of 0.1 nm and  
205 was highly collimated with a corresponding Full Width at Half Maximum (FWHM) (20  $\mu\text{m}$  (FWHM)  
206 vertically and 400  $\mu\text{m}$  (FWHM) horizontally) to reach a high spatial resolution in the vertical  
207 direction. The sample-to-detector distances were fixed to 2 m and 10 m. The SAXS measurements  
208 covered the following scattering vector range:  $2 \cdot 10^{-2} \text{ nm}^{-1} \leq q \leq 2 \text{ nm}^{-1}$ ,  $q = (4\pi/\lambda) \sin(\theta/2)$  and  $\theta$  is the  
209 scattering angle. The corresponding ( $\lambda = 2\pi/q$ ) length scale range is  $3.14 \text{ nm} \leq \lambda \leq 314 \text{ nm}$ . The  
210 filtration cell was mounted on motorized stages. A rotational stage was used to align the incident beam  
211 parallel with the membrane surface. A vertical translation stage allowed moving the filtration cell in  
212 front of the beam, in order to probe the structure at different vertical position. The incident beam  
213 passed through the sample in the filtration cell and the two-dimensional scattered intensity patterns  
214 were recorded on a high-resolution CCD detector (**Fig. 1 a, b**).

215 The analysis of the SAXS patterns registered in the cross-flow cell is the same which has already been  
216 described in preceding works [33, 34]. Four different zones were defined by measuring the transmitted  
217 X-ray signal as a function of the distance  $z_c$  through the SAXS cross flow filtration cell. The  
218 description of these zones has allowed to define the minimal distance  $z_c$  above which the scattered  
219 intensity is not influence by the X-ray beam partially crossing the polycarbonate permeate channel and  
220 the membrane. The detection of this minimal  $z_c$  position for which the scattered intensity can be  
221 properly registered (without influence of the polycarbonate permeate channel and the membrane) is  
222 fixed at zero ( $z_c = 0$ ). Thanks to a new design of the windows of observation and also with the use of  
223 the angular motion stage, the minimal distance above this  $z_c$  position for obtaining exploitable SAXS  
224 data was reduce to 20  $\mu\text{m}$ . To clarify the location of the zero position corresponding to the edge of the  
225 membrane surface, the description according to (Fig. 1 c) is the following: four areas are defined  
226 depending on the vertical distance in the filtration cell. A first zone Z1 correspond to the permeate  
227 channel in polycarbonate matter. The X- ray beam is totally absorbed in this region. A second area Z2  
228 is defined as being the membrane since a transmitted signal is received. This means that the X- ray  
229 beam starts to pass through the membrane, positioned onto the permeate channel. The signal increases  
230 for increasing vertical distance. In the third area Z3 the signal received is provided by the sample but  
231 is still affected by the membrane signal. This area measures a determined thickness depending on the  
232 beam width, here 20  $\mu\text{m}$ . When the scattering intensities received are constant, any influences from  
233 the membrane are detected and the area Z4 corresponding to the measure area is configured. So this  
234 area Z4 starts from 20  $\mu\text{m}$  above the membrane surface in our experiments and the  $z_c = 0$  position is  
235 fixed at the bottom of the area Z3 (Fig. 1 c).

236 Scattering patterns were normalized to an absolute intensity scale after applying standard detector  
237 corrections and then azimuthally averaged to obtain the one-dimensional intensity profiles denoted by  
238  $I(q)$ . Before the filtration experiments the cell was filled with demineralized water and the normalized  
239 background scattering associated was systematically subtracted to the scattering of suspensions during  
240 filtration experiments [33, 34].

241 An initial investigation of 5 suspensions of known volume fractions was performed in a flow through  
242 capillary cell 2 mm in diameter. This step allowed establishing the calibration curve of the absolute  
243 intensity as a function of the volume fraction. The results of the scattered intensity as a function of  
244 volume fractions allowed us to define the following linear relationship  $I(q = 0.6 \text{ nm}^{-1}) = 0.192 \phi_v$  [34].  
245 This equation has been established in the linear zone of the scattered intensity ( $q^{-2}$  power law decay)  
246 corresponding to the form factor of the dispersions, which indicates that it was not affected by the  
247 increasing mutual particle interaction (described by the structure factor of the dispersions) and  
248 therefore valid at high dispersion concentrations [33]. Indeed, the size of the Laponite clay is 30 nm in  
249 diameter and 1 nm in thickness. This size corresponds to  $q$  range, which defines the form factor of the  
250 scattering curve. This form factor does not vary with particle concentration. But at smaller  $q$  vectors,  
251 (larger distances than the particle sizes) the aggregation phenomena could change the scattering  
252 intensity as a function of the particle concentration (in a  $q$  vector range which is attributed to the  
253 structure factor) [33]. To properly extract the concentration from the scattering intensity, the analysis  
254 as to be done in the  $q$  range corresponding to the form factor, to determine the volume fraction as a  
255 function of the distance from the membrane.

256 Then, with the obtained calibration curve, the volume fraction of any Laponite suspension could be  
257 determined by introducing the corresponding absolute scattered intensity at a scattering vector  $q = 0.6$   
258  $\text{nm}^{-1}$ . This method has already been used [33-36] to determine the evolution of the volume fraction of  
259 the dispersions as a function of the distance  $z$  from the membrane. In other words, the concentration  
260 profiles in the accumulated layers during filtration were determined by this method. The scattering  
261 intensity for all the volume fractions reached within the concentrated particles layers at scattering  
262 vector  $q = 0.6 \text{ nm}^{-1}$  were in the  $q$  range where the scattering intensity is not affected by neither the  
263 structure factor nor the possible anisotropy of the SAXS pattern, as already discussed in a precedent  
264 work [33]. Following these results, *in-situ* SAXS measurements during Laponite clay suspensions  
265 filtrations were performed.

### 266 **2.3.2 *In-situ velocity field measurements during cross-flow ultrafiltration process***

267 Some relevant precedent work have proposed a methodology to predict pressure and velocity field in  
268 hollow fiber network of a filtration module [39]. The results were focalized on the effect of geometry  
269 of the module and the membranes, the membrane permeability as well as the operating filtration

270 conditions. The effects of shear forces induced by crossflow velocities on ex situ dead end filtration  
271 formed alginate fouling layer, were studied by crossflow experiments using multi slice multi echo  
272 imaging (MSME). The flow velocity measurements were performed to gain more insight into the  
273 hydrodynamics in the fouled membranes [39]. Nuclear magnetic resonance imaging (MRI) combined  
274 with MSME flow velocity measurements allowed further characterization of alginate layer structure  
275 and was used to elucidate the influence of  $\text{Ca}^{2+}$  on the fouling layer structure for alginate filtration  
276 within ceramic hollow fiber membranes. However, until now not any direct *in-situ* measurements of  
277 the flow field within the accumulated layers near the membrane surface during cross flow  
278 ultrafiltration, have been reported. Consequently, in this goal, a new cell was designed using Plexiglas  
279 (PMMA) to allow a complete visualization of the flow field along the feed channel. Micro-PIV  
280 technique was used to quantify the velocity field near the membrane surface during the filtration of  
281 Laponite suspensions. The dimensions of the feed channel were the same as for the cell used for  
282 SAXS filtration coupled experiments, The retentate channel was 100 mm long in x cross-flow flow  
283 direction and the flow section was 7.4 mm z high for 4 mm y large. The design of the cell allows  
284 performing micro-PIV measurements all along the length of the channel in the cross-flow flow  
285 directions (**Fig. 1d**). Then velocity profiles have been characterized in the same conditions and at the  
286 same x positions as those used for SAXS experiments. Micro-PIV measurements were performed with  
287 high-resolution camera synchronized with a pulsed laser. The laser used was a Nd:YAG pulsed with a  
288 wavelength of 532 nm and a power of 50 mJ/pulses (New Wave Solo). A specific lens was used to  
289 generate the thickness of the laser sheet depending on the flow and geometric characteristics. The  
290 thickness of this laser sheet was 1 mm. The laser sheet has been positioned in the middle of the canal  
291 in the y direction. Although the camera has a resolution of 2657 x 4000 pixels (Hisense 11M) with a  
292 cadency of 15 Hz, a visualization area of 2657 x 2000 pixels was used to optimize the storage size of  
293 the pictures. Polystyrene fluorescent particles 5  $\mu\text{m}$  in diameter (microParticle GmBh), with an  
294 absorbance and emission wavelength of 532 nm and 640 nm, respectively, were included in the  
295 filtrated Laponite suspension. Fluorescent particles were used in order to inhibit reflection  
296 phenomenon near the wall and surface membrane. The choice of tracers was the most suitable for our  
297 experiments and the Stokes number was  $8.6 \times 10^{-4}$ . The concentration in polystyrene fluorescent  
298 particles has been optimized to avoid any change in filtration performance or rheological behavior of  
299 the Laponite suspensions, and simultaneously permit suitable signals detected by the camera to get  
300 reliable correlation functions and velocity measurements.

301 The optical device was composed of a Canon 65 mm MPE lens linked to a filter (LaVision) with a  
302 range of 545 to 800 nm. The device is parameterized in order to the field of view be focused in the  
303 middle of the channel thickness in the y direction, corresponding to the laser sheet position. PIV  
304 processing requires a careful selection of interrogation window size to take into account robustness  
305 and accuracy for the calculation of the velocity especially in regions of high gradients. Adaptive PIV

306 approach leads to obtain the optimal local interrogation window size and shape based on flow  
307 gradients and image quality. The interrogation window size is varied according to the local flow  
308 gradient and the correlation value. Couples of images have been taken during the filtration time with a  
309 time laps between the first and the second image of couples corresponding of 150  $\mu\text{s}$  in average,  
310 taking into account the order of magnitude of the velocity (about  $0.06 \text{ m}\cdot\text{s}^{-1}$ ) to a particles  
311 displacement of 8 pixels on average, according to literature about that parameter [38]. Taking into  
312 account the order of magnitude of the velocity (about  $0.06 \text{ m}\cdot\text{s}^{-1}$ ) the time lap chosen corresponds to  
313 150  $\mu\text{s}$  in average. This time must be small enough to obtain a valid measure of the velocity and a  
314 certain length of displacement in the window of measure is required to quantify the velocity field. If  
315 the time laps are too high, particles will not be detected by the software from one picture to the other,  
316 and if the time laps are too small, the particles will not move enough and any displacement will be  
317 detected.

318 Commercial software “DynamicStudio” (Dantec) was used to extract the mean velocity fields from the  
319 recorded image frames. The processing principle is based on cross-correlation analysis of the particle-  
320 image patterns in small sub-domains between two successive image frames. To convert the pixel space  
321 into physical space, a calibration was performed using a specific target. Adaptive PIV processing  
322 requires a careful selection of interrogation window size to take into account robustness and accuracy  
323 for the calculation of the velocity especially in regions of high gradients. Adaptive PIV approach leads  
324 to obtain the optimal local interrogation window size and shape based on flow gradients and image  
325 quality. The interrogation window size is varied according to the local flow gradient and the  
326 correlation value.

327 The number of image frames (200 pairs of images) allowed a good convergence for statistical values  
328 of the velocity field. Due to high spatial-resolution of the camera, the measurements of the mean  
329 velocity components allowed an accurate quantification of the velocity gradients and the strain rate  
330 tensor each 30  $\mu\text{m}$  of distance above the membrane surface. An example of velocity profile obtained  
331 by this method is presented in **Fig. 1e**.

332

### 333 **3. RESULTS AND DISCUSSIONS**

#### 334 **3.1 Rheometric measurements**

335 From rheometric measurements, the flow curves (viscosity and shear stress as a function of the shear  
336 rate) are presented in **Figure 2** as a function of volume fraction and tspp content. The rheological  
337 behavior of the Laponite suspensions without tspp from 1 vol% to 3 vol% exhibits a shear thinning

338 behavior: the viscosity decreases while the shear stress increases with an increasing shear rate. The  
 339 yield stress behavior of the suspensions above a certain volume fraction is emphasis on (**Fig. 2b**) at  
 340 low shear rates  $0.1 \text{ s}^{-1}$ , the stresses reach a plateau value corresponding to the yield stress of the  
 341 suspensions. When the peptizer is added to the suspensions interparticular interactions are turned to  
 342 globally repulsive via linking to positive charges on the surface of the particles [40]. As discussed  
 343 before, the effect of this peptizer on the structure, rheological behavior, osmotic pressure and dead-end  
 344 filtration performance of the Laponite dispersions have been studied in details in our precedent works  
 345 [29, 33, 40]. The diphosphate anion binds the positive surface charge of the edges of the platelets. This  
 346 has the consequence to reduce the strength of edge-face and edge-edge attractions between the  
 347 particles. The result of this reduction in attractive forces between the particles is a partial disruption of  
 348 the network. As a consequence, the yield stresses measured for the same volume fractions are reduced  
 349 when the peptizer is added to the suspensions (**Fig. 2b**). For example, at 2 vol% the yield stress  
 350 without peptizer (L2-Cp0) is equal to 105 Pa and with peptizer (L2-CP6) the yield stress is reduced to  
 351 33 Pa (respectively open and closed square symbols in Fig 2b).

### 352 **3.2 Method for calculation of the shear stress profile within the accumulated layers,** 353 **during cross-flow ultrafiltration**

354 In the aim to calculate the stresses reach within the concentrated layers during the cross-flow  
 355 ultrafiltration process, an analysis of the rheometric flow curves (**Fig. 2**) has been made. This will  
 356 allow relating the shear rate to the shear stress by rheological laws. From the shear rate measured by  
 357 micro-PIV within the concentrated layers during the cross-flow ultrafiltration process, these equations  
 358 will allow to calculate the corresponding shear stress within the concentrated layers. The linear  
 359 regression of the experimental rheometric data (**Fig. 2b**) gives power law (eq. 1) or Herschel-Buckley  
 360 (eq. 2) laws depending on the volume fraction and peptizer content:

$$361 \quad \tau(\phi) = K(\phi) \cdot \dot{\gamma}^{n(\phi)} \quad (\text{eq. 1})$$

$$362 \quad \tau(\phi) = K(\phi) \cdot \dot{\gamma}^{n(\phi)} + \tau_s(\phi) \quad (\text{eq. 2})$$

363 Where  $\phi$  is the volume fraction (vol%),  $\tau(\phi)$  is the shear stress (Pa),  $\dot{\gamma}$  the shear rate ( $\text{s}^{-1}$ ),  $K(\phi)$  is the  
 364 consistency,  $n(\phi)$  the shear thinning index, and  $\tau_s(\phi)$  is the yield stress.

365 From the fitted laws, the expressions of  $K$  and  $n$  and  $\tau_s$  as a function of the volume fraction are  
 366 deduced (eq. 3 to 8).

367 For Laponite suspensions with peptizer, the expressions for  $K$ ,  $n$  and  $\tau_s(\phi)$  are the following:

$$368 \quad K(\phi) = 64318 \times \phi^{2.396} \quad (\text{eq. 3})$$

369 
$$\mathbf{n}(\phi) = 500 \times \phi^2 - 30 \times \phi + 0.65 \quad (\text{eq. 4})$$

370 
$$\tau_s(\phi) = 1.046 \times 10^6 \times \phi^{2.69} \quad (\text{eq. 5})$$

371 For Laponite suspensions without peptizer, the expressions for  $\mathbf{K}$ ,  $\mathbf{n}$  and  $\tau_s(\phi)$  are the following:

372 
$$\mathbf{K}(\phi = 1) = 0.968 \quad (\text{eq. 6})$$

373 
$$\mathbf{n}(\phi = 1) = 0.39 \quad (\text{eq. 7})$$

374 
$$\tau_s = 1.592 \times 10^9 \times \phi^{4.27} \quad (\text{eq. 8})$$

375 From the velocity profiles ( $\mathbf{V}(z)$ ) obtained by micro-PIV the following expression (eq. 9) gives access  
376 to a calculation of the corresponding shear rate:

377 
$$\dot{\gamma}(z) = \frac{dV}{dz} \quad (\text{eq. 9})$$

378 With  $z$  the distance from the membrane surface (m), and  $\mathbf{V}$  the measured velocity ( $\text{m}\cdot\text{s}^{-1}$ ).

379 For each filtration condition during time and distance  $z$  from the membrane surface, it is then possible  
380 to calculate the shear stress within the concentration polarization (eq. 10), thanks to the knowledge of  
381 i) the value of the volume fraction measured by SAXS, ii) the value of the calculated shear rate  
382 deduced from the micro-PIV (eq. 9) and iii) the rheological laws ( $\phi$ ) (eq. 3 to 8). It is important to  
383 notice here that one assumption is made which consider that rheological behavior of concentration  
384 polarization and gel layers of Laponite in the cross-flow experiment is equivalent to those of bulk  
385 Laponite suspensions having same particle concentration. It will be difficult to verify this assumption  
386 as any direct measurements with a specific probe, introduce in the flow, will modify the measuring  
387 stresses.

388 
$$\tau(\phi, z) = \mathbf{K}(\phi) \cdot \dot{\gamma}(z)^{\mathbf{n}(\phi)} + \tau_s(\phi, z) \quad (\text{eq. 10})$$

389 For Laponite suspensions without peptizer, the rheological behavior is shear thinning only for 1 vol%.  
390 For higher volume fractions, the expression of the shear stress (eq. 10) can be replace only by the  
391 expression of the yield stress corresponding to this kind of suspension, because  $\mathbf{n}(\phi > 1) = 0$  and  
392  $\dot{\gamma}(z)^{\mathbf{n}(\phi > 1)} = 0$ . So for  $\phi > 1$  vol%, (eq. 10) equals (eq. 8).

393 **3.3 *In-situ* Concentration profiles during cross-flow ultrafiltration: SAXS analysis,**  
394 **relaxation phenomena and lowering of the membrane**

395 **a) SAXS Analysis.** To investigate the accumulation phenomena during cross-flow ultrafiltration,  
396 different filtration condition steps have been explored. In a first step, under a transmembrane pressure  
397 of  $1.1 \times 10^5$  Pa a cross-flow of  $0.3 \text{ L}\cdot\text{min}^{-1}$  has been applied and the structural organization and

398 concentration profiles deduced by SAXS have been recorded during time (**Fig. 3a**). In a second step,  
399 under the same pressure conditions the cross-flow has been reduced to  $0.06 \text{ L}\cdot\text{min}^{-1}$  in order to  
400 emphasis the phenomena in a regime for which critical conditions (limiting flux) are reached as shown  
401 previously in details in previous works [33]. The corresponding concentration profiles (**Fig. 3b**)  
402 deduced from the SAXS measurements (**Fig. 3c and d**) show a continual increase in concentration as  
403 a function of  $z$  and filtration time. On (**Fig. 3c**) are plotted the scattering intensities  $I(q)$  as a function  
404 of the  $q$  vector for different distances registered in-situ inside the crossflow ultrafiltration cell as a  
405 function of distance  $z$ , at filtration time  $t = 94 \text{ min}$  of step 2. This curve show the increase of the whole  
406 scattering intensity curve at decreasing distances  $z$  toward the membrane in relation with the increase  
407 of particle concentration. The corresponding Kratky plot representation ( $q^2 \cdot I(q)$ ) is plotted in (**Fig.**  
408 **3d**). Kratky plot is another way to represent scattered intensities, emphasizing the variation of  
409 scattering intensities (slopes and local maximum) as a function of  $q$  vectors. Peaks can be observed at  
410 a certain  $q_{\text{max}}$  wave vector which correspond to a maximum of scattering intensity. This  $q_{\text{max}}$  position  
411 correspond to a mean inter-particle distance  $d = 2\pi/q_{\text{max}}$  [29, 33] Fig. 3d show that the  $q_{\text{max}}$  position is  
412 increasing at decreasing  $z$  distances which **emphasizes** the fact that inter-particle distances  $d$  decreases  
413 as concentration increase toward the membrane surface.

414 **b) Lowering of the membrane.** In a third step, to explore the relaxation phenomenon during time and  
415 the dynamic of the change in structural organization and concentration evolution, the cross-flow was  
416 stopped and the pressure was released. In this arrested state, the SAXS measurements were  
417 continuously registered as a function of the distance  $z_c$  and time (**Fig. 4 a**). Thanks to this relaxation  
418 step, a specificity of our experimental setup was emphasized. In our experimental set-up the  
419 membrane is not supported by any porous rigid media, which has induced an effect of lowering of the  
420 membrane in the permeate channel due to the effect of transmembrane pressure. **Fig. 4 a** compares the  
421 scattering intensities inside the accumulated layers just before and after the time when the cross-flow  
422 was stopped and the pressure was released. A sudden jump in the scattering intensity in the upper  
423 distances has been highlighted. This sudden increase of the corresponding calculated concentration  
424 profile is due to the fact that without transmembrane pressure, the membrane has now the ability to de-  
425 stress and recover its initial flat form, which allowed now to let appear in front of the beam from  $z_c = 0$   
426 position, the whole concentration profile from its surface. In this relaxed configuration the  $z_c = 0$   
427 position correspond to the distance  $z$  from the membrane surface as the membrane is not lowered  
428 anymore. Many measurements on different samples have allowed checking this phenomenon of  
429 lowering of the membrane under pressure and de-stress of the membrane when the transmembrane  
430 pressure is released. All the measurements gives the same sudden change of the concentration profile  
431 which is shift  $350 \mu\text{m}$  above the  $z_c = 0$  position. In order to take into account this lowering of the  
432 membrane, all the results presented thereafter, under transmembrane pressure, will be plotted as a

433 function of the distance  $z$  from the membrane surface named  $z$  ( $\mu\text{m}$ ) in the graphs, where  $z = z_c + 350$   
434  $\mu\text{m}$ .

435 The consequence of this observation is twofold: firstly it has allowed us to evidence that the first  
436 layers deposited near the membrane surface during filtration reach higher concentration levels and  
437 better orientated states than initially detected (**Fig. 3**). Secondly, it has allowed us to define the  
438 effective  $z$  distance from the membrane surface ( $z = z_c + 350 \mu\text{m}$ ). In order to take into account this  
439 lowering of the membrane, all the concentration profiles in the next figures were shifted by  $350 \mu\text{m}$   
440 from the measured  $z_c$  position. It is important to notice that this phenomenon of lowering of the  
441 membrane has been emphasized also in micro-PIV measurements performed with an equivalent set-  
442 up, so that the concentration profiles and the velocity profiles deduced by micro-PIV can be related  
443 one to each other as they are finally registered in the same membrane position conditions.

444 **c) Description of the relaxation phenomena.** During the relaxation, the concentration profiles  
445 evolves (**Fig. 4 a**) from a gradient of concentration with an exponential trend as a function of  $z$ ,  
446 towards a flat concentration profile near the membrane surface on time scales of about half an hour.  
447 This relaxation phenomena could be interpreted as a diffusion process of the concentrated particles  
448 accumulated near the membrane surface (hundreds of micrometers) towards the lowest concentrated  
449 layers in the upper part of the accumulated layers on distances of thousands of micrometers length  
450 scale.

451 Regarding the scattering patterns evolutions (**Fig. 4 b**) at relaxation time  $t = 2$  min the scattering  
452 patterns are anisotropic near the membrane surface at  $z = 20 \mu\text{m}$  and become more and more isotropic  
453 at increasing distances  $z$ . This anisotropy of the scattering pattern is induced by a parallel orientation  
454 of the particles along the membrane surface during the filtration under the effect of transmembrane  
455 and shear flow forces as already described [33]. After cessation of flow and release of the pressure this  
456 orientation slowly disappear, for example the scattering patterns at position  $z = 20 \mu\text{m}$  becomes more  
457 and more isotropic at relaxation times 9, 20 and 30 minutes. This decrease in anisotropy is also visible  
458 as a function of distance  $z$  for a certain relaxation time. Finally, at relaxation time  $t = 30$  minutes, all  
459 the scattering patterns are isotropic for each distance  $z$ , denoted a complete relaxation of the  
460 orientations in relation with a flattening of the concentration profile. The concentration is almost the  
461 same around 3 vol% from  $z = 0$  to  $1200 \mu\text{m}$ .

462

### 463 **3.4 Concentration profiles deduced from *in-situ* SAXS,**

464 **Laponite suspension with peptizer:** After one step of filtration at  $0.3 \text{ L}\cdot\text{min}^{-1}$  (step 1) during 80 min  
465 **Fig 5 a** shows the results of accumulation during step 2 at a flow rate of  $0.06 \text{ L}\cdot\text{min}^{-1}$ , for a Laponite

466 suspension with peptizer (L1-Cp6). The volume fraction increases near 350  $\mu\text{m}$  above the membrane  
467 surface and by further distance from this reference at increasing filtration times. At the beginning of  
468 this step 2, the volume fraction near 350  $\mu\text{m}$  above the membrane is around 1.8 vol% (**Fig. 5 a**). After  
469 94 min of filtration, the volume fraction reaches 5 vol% near the membrane and the thickness of the  
470 concentrated layer formed during the process reaches 950  $\mu\text{m}$ . The SAXS patterns show an increase of  
471 the oval shape for closer distances from the membrane surface than for further distances. This non  
472 circular shape in the vertical direction means that a horizontal orientation within the colloidal particles  
473 aggregated at the membrane surface is induced by the increase of the concentration during the cross-  
474 flow filtration. Above a distance of 1000  $\mu\text{m}$  where no particles accumulation is detected, the SAXS  
475 pattern shows a circular shape, meaning that there is no preferential orientation.

476 **Laponite suspension without peptizer:** After one step of filtration at 0.3  $\text{L}\cdot\text{min}^{-1}$  (step 1) during 70  
477 min and then one step at 0.2  $\text{L}\cdot\text{min}^{-1}$  during 57 min (step 2), **Fig 5 b** shows the results of accumulation  
478 during step 3, at a flow rate of 0.06  $\text{L}\cdot\text{min}^{-1}$ , for the Laponite suspension without peptizer. The  
479 concentrated layer is thicker and the volume fraction reaches a higher value than for Laponite without  
480 peptizer. As for a suspension of Laponite with peptizer, the SAXS patterns after 81 min of filtration  
481 (Fig. 5b) show an increase in the orientation for closer distances from the membrane surface during  
482 the process. It is worth noting that the concentrated layer is thicker for the suspension without peptizer  
483 due the ease of the particles to create aggregates. This observation confirms the role played by the  
484 interparticular interactions and the rheological behavior in the build up of the concentrated layers.

### 485 3.5 Velocity field deduced from the *in-situ* micro-PIV

486 A first set of experiments was conducted to characterize the permeation flux evolutions as a function  
487 of cross-flow conditions at increasing transmembrane pressures. The goal is to evaluate if the limiting  
488 flux is reached or not. In this first experiment, a constant cross-flow is maintained and an increasing  
489 transmembrane pressure was applied for the dispersions with and without peptizer. For each  
490 transmembrane pressure applied, the permeation flux was recorded until reaching a steady state value  
491 after an average value of 25 minutes. The steady state permeation flux  $J$  is plotted in **Figure 6** for the  
492 different cross-flow conditions investigated in this article. For all these conditions the limiting flux is  
493 reached for a higher permeation flux of about  $6 \text{ L}\cdot\text{h}^{-1}\cdot\text{m}^{-2}$  for the higher cross-flow conditions ( $Q = 0.3$   
494  $\text{L}\cdot\text{min}^{-1}$ ) compared to about  $2.5 \text{ L}\cdot\text{h}^{-1}\cdot\text{m}^{-2}$  for the lower cross-flow conditions ( $Q = 0.06 \text{ L}\cdot\text{min}^{-1}$ ). In the  
495 following some measurements of the shear velocity field have been performed for all these cross-flow  
496 conditions, and give the same features. In order to keep concise presentation, only the results at ( $Q =$   
497  $0.06 \text{ L}\cdot\text{min}^{-1}$ ) are presented. The same phenomena are observed during the filtration step 1 with a flow  
498 rate of  $Q = 0.3 \text{ L}\cdot\text{min}^{-1}$  for the Laponite suspension with peptizer, and the filtration step 1 and 2 for the  
499 Laponite suspension without peptizer. The velocity profiles show the reduction of the velocity near the  
500 membrane surface for increasing time of filtration and show the formation of the concentrated layers

501 during the time of filtration and as a function of the flow rate. Indeed, when the flow rate is decreased,  
502 the velocity profiles show a higher area with any measurement of flow than for a high flow rate.

503 **Suspensions of Laponite with peptizer:** Because of previous filtration steps to highlight the effect of  
504 the hydrodynamic condition on the formation of the concentrated layers, the velocity profile at the  
505 beginning of the filtration step 2 at  $Q = 0.06 \text{ L}\cdot\text{min}^{-1}$ , does not show any velocity at the surface of the  
506 membrane and an area of no velocity of  $700 \mu\text{m}$  above the membrane surface (**Fig. 7 a**). The  
507 corresponding permeation flux measured in-situ (**Fig. 7 b**) continuously decreases and stabilizes  
508 around  $2.5 \text{ L}\cdot\text{h}^{-1}\cdot\text{m}^2$  at time  $t = 22 \text{ min}$  until the end of the experiment. For increasing filtration times,  
509 PIV results show an increasing thickness of the area of no velocity near the membrane surface. At the  
510 end of this filtration step, any velocity is detected over a distance of about  $900 \mu\text{m}$  above the  
511 membrane instead of  $700 \mu\text{m}$  at the beginning of this step. This is important to notice that the velocity  
512 profile starts to stabilize since 90 minutes of filtration whereas 22 minutes are enough to show a  
513 stabilization of the permeate flux. the stabilization of the upper flowing layers (from time  $t = 22 \text{ min}$  to  
514  $t = 140 \text{ min}$ ) will affect not to much the permeation flux as the corresponding changes in concentration  
515 are lower than the one in the more concentrated stagnant layer. This emphasis the fact that the most  
516 important resistance inducing a flux reduction is due to the stagnant concentrated layer near the  
517 membrane surface. This result agrees with SAXS experiment results which show an increasing volume  
518 fraction near the membrane surface for increasing filtration times. [We can conclude that the reduction](#)  
519 [of the velocity is linked to the increase in volume fraction, which conduct to an arrested state of the](#)  
520 [suspensions in the most concentrated layers near the membrane surface.](#)

521 **Suspensions of Laponite without peptizer:** in the same way, for the last filtration step3 with a low  
522 flow rate of  $Q = 0.06 \text{ L}\cdot\text{min}^{-1}$  (**Fig. 7 c**) the same phenomenon is observed. The region of no velocity  
523 has grown for increasing filtration times, even if the permeate flow  $J$  has reached a permanent state  
524 (**Fig 7 d**). At the end of the filtration, a concentrated layer of  $2100 \mu\text{m}$  (higher than the one reported  
525 with  $t_{\text{sp}}$ ) is formed at the membrane surface.

526

### 527 **3.6 Shear rate fields within accumulated layers during cross-flow ultrafiltration**

528 **Figures 8 a) and b)** show shear rate profiles calculated from velocity PIV measurements during the  
529 time of filtration of a suspension of L1-Cp6 (**Fig. 8 a**) and for a suspension of Laponite without  
530 peptizer L1-CP0 (**Fig. 8 b**) during, respectively, the step 2 and the step 3 of filtration at  $0.06 \text{ L}\cdot\text{min}^{-1}$   
531 flow rate, corresponding to a limiting flux previously described (**Tab. 1 and Fig. 6**).

532 These shear rate profiles exhibit three different evolutions as a function of the distance  $z$  from the  
533 membrane surface. Firstly, a zero value corresponding to the area of no velocity near the membrane

534 surface is observed as shown in **Fig. 7**. Secondly, an increase in the shear rate as a function of  $z$  is  
535 reported (Fig 8a and b) which corresponds to the increase in the velocity until reaching a maximum.  
536 Thirdly a decrease in the shear rate until reaching a lower value corresponding to an area where the  
537 velocity field reaches middle of the cell in  $z$  position is noted. For higher filtration times, the observed  
538 phenomena are the same with a difference in the thickness of the area of no flow; a change in the  
539 maximum value and position of the shear rate, which is in accordance with the fact that the  
540 concentrated layer becomes thicker for increasing filtration times and decreasing flow rate, in  
541 agreement with the previous SAXS and micro-PIV results.

542 For the suspension with peptizer, **Figure 8 a** shows a high shear rate of about  $140 \text{ s}^{-1}$  near  $700 \mu\text{m}$   
543 above the membrane surface at the beginning of the filtration step ( $t=0 \text{ min}$ ), which corresponds to the  
544 shear of the suspension at the initial filtered concentration ( $\phi = 1 \text{ vol } \%$ ). Indeed, at  $700 \mu\text{m}$  above the  
545 membrane surface, fig. 5a shows for time  $t = 0 \text{ min}$  of this filtration step, that the concentration is the  
546 initial value of the suspension, which means that any increase in concentration is detected at this  
547 distance on  $z$  direction. The shear properties of Laponite suspension correspond to a shear thinning  
548 behavior with a shear thinning index  $n = 0.4$  according to eq. 4. After 60 and 90 min filtration, the  
549 maximum value of the shear rate decreases and is positioned at increasing  $z$  levels. This evolution is in  
550 accordance with the formation of a higher concentrated and thicker layer during the filtration process  
551 as shown in **Figures 5 and 7**.

552 For the suspension without peptizer, for the same filtration conditions the maximum of the shear rate  
553 profile is positioned at higher  $z$  position ( $1500 \mu\text{m}$  above the membrane surface) than with peptizer,  
554 and the shear rate maximum value ( $60 \text{ s}^{-1}$ ) is lower than with peptizer. This is in accordance with the  
555 fact that the filtration of the Laponite suspension without peptizer forms a thicker and more  
556 concentrated layer than without peptizer, as shown in **Figures 5 b and 7 c**. Nevertheless, at increasing  
557 filtration times the maximum value of the shear rate increases, contrary to the case with peptizer. This  
558 emphasises a more complex phenomenon certainly related to the more complex thixotropic  
559 rheological of the Laponite dispersions without peptizer. One way to better understand these  
560 evolutions is to link the shear rate, velocity and concentration profiles to the rheological behavior of  
561 the suspensions as a function of their volume fraction.

### 562 **3.7 Shear stress fields within accumulated layers during cross-flow ultrafiltration**

563 To understand the concentration polarization phenomena, we will take advantage of the combined  
564 results obtained by SAXS and micro-PIV on the same suspensions in the same filtration procedures  
565 which have allowed to get access to the velocity shear rate and concentration profiles as a function of  
566 the distance  $z$  from the membrane surface. Combining all these results with the rheological behavior of  
567 the suspensions, we had the opportunity to calculate the shear stresses inside the concentrated layers as

568 described in part 3.2 of this article. The only assumption made is that the rheological behavior of  
569 concentration polarization and gel layers of Laponite in the cross-flow experiment is equivalent to  
570 those determined by rheometric measurements for Laponite suspensions having the same particle  
571 concentration.

572 **Figure 9 a** shows the shear stress profiles calculated for increasing filtration times as a function of the  
573 distance  $z$  from the membrane surface of a Laponite suspension with peptizer during the last step 3 of  
574 filtration at  $Q = 0.06 \text{ L}\cdot\text{min}^{-1}$ . This result shows that the stress near  $350 \mu\text{m}$  above the membrane  
575 increases during the filtration time due to the formation of the concentrated layer. For the 3 different  
576 times of filtration presented, the shear stress profile has the same behavior: a first area where the stress  
577 value decreases in link with firstly the decrease in volume fraction at increasing  $z$  and secondly in link  
578 with the area of no flow measured by micro-PIV (**Fig. 7 a**) and (**Fig. 8 a**). The values of shear stress  
579 calculated for this area correspond to the yield stress value. **Figure 10 a** locate the calculated shear  
580 stress in the concentrated layers during the filtration, on the shear stress/shear rate flow curve of the  
581 suspension as a function of the volume fraction. The stresses reach in this decreasing part of the shear  
582 stress (**Fig. 9a**) are located in the yield stress domain of the flow curve of the suspension. After this  
583 first area of decreasing stress, the evolution of the shear stress profile reaches a plateau with a constant  
584 value for increasing filtration times. In this area above  $z = 1000 \mu\text{m}$ , the volume fraction of the  
585 suspension reaches the initial filtered suspension 1 vol% and the shear rate stabilizes towards its lower  
586 value.

587 **Figure 9 b** shows the calculated shear stress profiles during the last filtration step3 for a suspension of  
588 Laponite without peptizer. The shear stress profiles show the same behavior during the time of  
589 filtration for L1-Cp0 suspensions and L1-Cp6 suspensions. Nevertheless, near the membrane surface,  
590 the stress has a higher value than with peptizer (from 500 Pa to 8000 Pa depending on the filtration  
591 time) and decreases until reaching a plateau at a constant value around 10 Pa, for the 3 different  
592 filtration times. As previously seen for a suspension of Laponite with peptizer, the shear stress  
593 measured near the membrane surface (before the plateau) corresponds to the stresses obtained when no  
594 flow is measured by micro-PIV in the concentrated layer, and thus corresponds to the yield stresses.  
595 **Figure10 b** shows the location of the stress calculated from the velocity profiles in the concentrated  
596 layer, on shear stress/shear rate flow curve of the suspension without pepetizer as a function of the  
597 volume fraction measured by rheometric measurements. It appears that the stress obtained for a  
598 suspension of Laponite without peptizer has a higher value than for a suspension of Laponite with  
599 peptizer in accordance with the change in the rheological behavior due to the modification in  
600 interparticular interactions. Starting from the same volume fraction of 1 vol % and following the same  
601 filtration procedure in the same conditions, the changes observed in the concentration, velocity and  
602 stresses profiles in the concentrated layers for the suspensions with and without peptizer, are linked to

603 the change in the rheological behavior. One of the principal change in this behavior is the sol/gel  
604 volume fraction transition. Without peptizer the sol/ gel transition is around 1 vol%, while with  
605 peptizer, the sol/gel transition is between 1 and 2 vol%. This has a huge consequence on the way the  
606 particles concentrate near the membrane surface submitted simultaneously to shear, pressure and  
607 colloidal forces. Another interesting point is that as already shown in previous papers [33, 34] the  
608 osmotic pressure of the Laponite suspensions with and without peptizer follows the same dependence  
609 with the volume fraction, same equation of state. The differences emphasized in these results for the  
610 suspensions with and without peptizer reinforce the precedent conclusions [33], namely that the  
611 pertinent parameter which control the filtration performance is the hydrodynamic/rheological behavior  
612 of the suspension and even though the osmotic pressure evolution is an important parameter of the  
613 filtration, it is not the most important parameter in this kind of colloidal suspensions.

### 614 **3.8 Concentrated layers behavior: relationship with rheological behavior of the** 615 **suspensions**

616 In this section we will analyze the effect of the rheological behavior on the formation of the  
617 concentrated layer and the influence on the hydrodynamic field, structural organization and the stress  
618 field applied near the membrane surface. From the whole data and calculations obtained in this article,  
619 **Figures 11 and 12** summarize and compare on the same figure the volume fraction (red empty circles  
620 curve), calculated shear stress (black full circles curve) and calculated shear rate (blue full triangles  
621 curve) as a function of the distance  $z$  from the membrane surface. For each suspension with peptizer  
622 (**Fig. 11**) and without peptizer (**Fig. 12**) these profiles have been plotted for three different filtration  
623 times, in the same cross-flow and transmembrane pressure conditions. The calculations have been  
624 done from the SAXS and micro-PIV measurements performed mostly at the same filtration time. For  
625 example for the results presented in Fig. 11, the calculations are done from the volume fractions  
626 deduced from SAXS experiments (Fig. 5a) at filtration time ( $t = 0$  min,  $t = 59$  min and  $t = 94$  min) and  
627 the calculated shear rates and shear stress from the micro-PIV measurements (Fig. 7 a) at the related  
628 filtration times ( $t = 0$  min,  $t = 60$  min,  $t = 90$  min). *These two set of data from SAXS and micro- PIV  
629 experiments are recorded at namely the same filtration times. The largest difference of recording times  
630 between the SAXS and micro-PIV data is 5 minutes. As the phenomena of accumulations are slower:  
631 the whole accumulation phenomena is on the order of 100 minutes, this small difference of 5 minutes  
632 in recording times will negligibly affect the calculation of the shear stress. Consequently, the  
633 conclusions on the whole concentration phenomena and trend of the calculated shear stress as a  
634 function of  $z$  or filtration time, will not be affected by this difference of recording times.*

635 These combined results and calculations allow to highlight three different regions (A, B, C) from the  
636 membrane surface to the feed channel, with different specific behaviors in terms of rheological and  
637 filtration accumulation.

638 **Laponite suspensions with peptizer (L1-Cp6): Figures 11 a), b) and c)** exhibit the three different  
639 regions (A, B, C) at different times of filtration, respectively  $t = 0$  min,  $t = 60$  min and  $t = 90$  min. At  
640 the beginning of step 2 of filtration at  $Q = 0.06 \text{ L}\cdot\text{min}^{-1}$ , the volume fraction is the same as the volume  
641 fraction measured at the end of the previous filtration step 1 at  $Q = 0.3 \text{ L}\cdot\text{min}^{-1}$ , as shown in **Figures 3**  
642 **a) and b).**

643 In the first region called A which extends up to  $500 \mu\text{m}$ , the velocity and shear rate are close to zero,  
644 corresponding to a suspension at rest. This means that the calculated stress, which corresponds to the  
645 yield stress, is not high enough to give rise to a flow inside the concentrated layer. This region matches  
646 with the fouling layer, with a decreasing stress while the volume fraction decreases, in agreement with  
647 the rheometry measurements (**Fig. 10 a**). At the beginning of the second region called B, the shear rate  
648 and corresponding calculated shear stress start to increase until reaching a maximum value of  $7 \text{ Pa}$   
649 when the shear rate maximum is about  $135 \text{ s}^{-1}$ . In this region B the shear flow forces are sufficiently  
650 high, compare to colloidal interactions and pressure forces, to initiate the flow of the suspension. This  
651 region B can be assimilated to the concentration polarization layer. The third region called C appears  
652 when the shear rate starts to decrease until reaching a minimum value. In this region C, the volume  
653 fraction is constant and equal to the initial volume fraction  $1 \text{ vol}\%$ , the shear rate decreases with the  
654 corresponding shear stress until reaching the conditions where the suspension is circulating in the feed  
655 channel. This region C is out of the concentration phenomena and corresponds to the flowing layer  
656 above the concentration polarization layer (region B).

657 After 60 and 90 mins of filtration corresponding to **Figures 11 b) and c)**, the same phenomena are  
658 observed but over a higher  $z$  distance range due to accumulation of particles. The values of the  
659 calculated shear stresses near the membrane surface increases when increasing the volume fraction for  
660 fixed distances depending on the filtration time. Near  $350 \mu\text{m}$  above the membrane surface, the stress  
661 reaches  $200 \text{ Pa}$  after 60 min of filtration (**Fig. 11 b**) and  $300 \text{ Pa}$  after 90 min of filtration (**Fig. 11 c**) in  
662 the fouling layer (region A). When the shear rate increases (region B), the required stress to involve a  
663 flow is about  $40 \text{ Pa}$  at 60 min and 90 min of filtration. This critical stress value to initiate the flow has  
664 the same value because this phenomenon appears when the volume fraction is between  $1$  and  $2 \text{ vol}\%$ ,  
665 corresponding to the sol/gel volume fraction transition for a suspension of Laponite with peptizer. The  
666 value of the shear rate and shear stress far away from the membrane ( $z = 2000 \mu\text{m}$ ), are the same at  
667 time  $t = 60$  min and  $t = 80$  min which shows that this region of the flowing suspensions is not  
668 influenced anymore by the concentrated lower layers.

669 **Laponite suspensions without peptizer (L1-Cp0):** In the case of Laponite suspensions without  
670 peptizer the three regions A, B and C are also well identified but extend on higher  $z$  distances from the  
671 membrane surface (**Fig. 12 a**). In the first region A corresponding to the fouling layer, the calculated  
672 stress decreases as a function of  $z$  as a consequence of the decrease in volume fraction, and the stress

673 corresponds to the yield stress of the suspensions. When the filtration time increases (**Fig. 12 b and 12**  
674 **c**), the thickness of the fouling layer (region A) increases within higher values of shear stress due to  
675 the increase of volume fraction during the time of filtration. The stress level can reach high values at  
676 time  $t = 80$  min of filtration, as high as 5000 Pa for a corresponding volume fraction of 20 vol% at  $z =$   
677  $350 \mu\text{m}$ . It is interesting to underline that in this region A, the volume fraction decreases until reaching  
678 the initial volume fraction of 1 vol% at  $z = 1150 \mu\text{m}$  for filtration time  $t = 35$  min (**Fig. 12 b**) and at  $z =$   
679  $1360 \mu\text{m}$  for filtration time  $t = 80$  min (**Fig. 12 c**), then the stress becomes flat and corresponds to  
680 the yield stress 5 Pa of the Laponite suspensions.

681 In the region B the maximum shear rate obtained in this concentration polarization layer is higher at  
682 the end of the filtration than at the beginning (almost  $80 \text{ s}^{-1}$  instead of  $60 \text{ s}^{-1}$  at the beginning) because  
683 the velocity profiles associated show more brutal changes for increasing filtration times. Indeed, the  
684 thickness of the concentrated layer increases for increasing filtration times and the mean flow velocity  
685 is more important for larger distances from the membrane surface. Therefore, during the time of  
686 filtration when the particles leave the accumulated layer to be introduced in the flow, the velocity that  
687 they will adopted will be more important on shorter distances during the time of filtration.

688 The change between region A and B is not only related to the static yield stress of the suspension but  
689 also to the shear history of the suspension of this thixotropic system. Consequently, for the two  
690 different filtration times the limit between these two regions A and B is pushed towards higher  $z$   
691 values, at increasing filtration times. At 0 min filtration time this limit is at  $z = 1030 \mu\text{m}$  and shifts to  $z =$   
692  $1400 \mu\text{m}$  at  $t = 35$  min until  $z = 1700 \mu\text{m}$  at  $t = 81$  min. It is then necessary to take into account the  
693 complex relationships between the restructuring level of the Laponite suspensions and the stresses  
694 applied by the upper flowing layers which are higher at increasing  $z$  distances.

695 Another interesting point is that in this region B, the maximum value of the shear rate reached without  
696 peptizer, is lower than for a suspension of Laponite with peptizer, in agreement with the fact that for  
697 the same volume fraction 1 vol%, the viscosity of the suspension without peptizer is higher than the  
698 one with peptizer. The required stress to involve a flow at the interface between the fouling and the  
699 concentration polarization layers is weaker for a Laponite suspension without peptizer than when the  
700 peptizer is added. This is mostly explained by the difference of the sol/gel volume fraction transition  
701 that depends on the presence of the peptizer. When the peptizer is mixed to the suspension, the sol/gel  
702 volume fraction transition is higher than without peptizer and according to the rheometric  
703 measurements, the yield stress is more important for increasing volume fractions.

704 These observations emphasize the fact that for the same filtration conditions, same cross-flow and  
705 same transmembrane pressure, the stresses inside the concentration polarizations layers adjust their  
706 values in order to find an equilibrium between the external forces imposed by the cross-flow (which

707 tend to disrupt the structure) and the resistance forces (which tend to build up the structure related to  
708 internal forces of the suspension). In the particular case of this thixotropic colloidal suspension these  
709 internal colloidal forces are a complex combination of the colloidal interaction between the particles,  
710 the history of the previous shear and pressure forces applied, which could have disrupted the structure of  
711 the suspensions and weaken the interparticle forces as a function of time. These time-dependent  
712 evolutions (break-down and build-up) of the structure are highly dependent on the volume fraction of  
713 the particles and also on the modification of the surface forces between the particles (with peptizer or  
714 not) as already shown [33] Consequently during the filtration process, under a constant cross-flow and  
715 transmembrane pressure, starting from an initial volume fraction, the final equilibrium concentration  
716 polarization layer reached is the consequence of the way the particles (starting from a certain  
717 structuring state) start to accumulate and concentrate during time. It has been previously shown that  
718 the concentration of the particles within the accumulated layers follow an exponential trend as a  
719 function of distance  $z$  from the membrane surface as well as a function of filtration time [34]. Each  
720 layer of the Laponite suspension at each volume fraction has a certain "destructuring" or restructuring  
721 time. It is then a complex combination of this restructuring time (at each sublayer with a given volume  
722 fraction) in competition with the destructuring time imposed by the cross-flow, which at the end, result  
723 in a certain stabilized concentration polarization layer. These time- and spatial-dependent phenomena  
724 are well emphasized in **Figures 11 and 12**, for which in the same filtration conditions (cross-flow and  
725 transmembrane pressure) the two different suspensions (with and without peptizer) in terms of  
726 interparticle interactions and consequently rheological behavior, give rise to different equilibrium  
727 concentration layers. Nevertheless, it is important to claim that the mechanisms involved for these two  
728 different suspensions are the same with the existence of the three same behaviors associated to the  
729 three regions A, B and C.

730

## 731 CONCLUSIONS

732 This work combines *in-situ* SAXS, *in-situ* micro-PIV and rheological measurement to bring a better  
733 understanding of the time and spatial-dependent behavior of the concentrated layer near the membrane  
734 surface during the ultrafiltration process of Laponite suspensions. The structural and kinematic  
735 evolutions of the concentrated layers have been linked to the rheological behavior evolutions of the  
736 filtered suspensions.

737 The results of SAXS experiments performed *in-situ* during the filtration process have allowed  
738 highlighting the exponential increase of the volume fraction as a function of the distance  $z$  from the  
739 membrane surface as well as a function of the filtration time. The obtained results revealed the  
740 importance of the level and the type of electrostatic interactions between the particles in the

741 mechanism of formation of the concentrated layers. The Laponite suspensions without peptiser,  
742 namely in attractive particle interactions, give rise at equilibrium to a thicker and more concentrated  
743 layers than the suspensions with peptisant in repulsive particles interactions.

744 The original micro-PIV characterization performed within the accumulated layers during the crossflow  
745 ultrafiltration of colloids allowed giving access to the velocity field as a function of the distance  $z$   
746 from the membrane surface. Thanks to rheometric measurements, the rheological behaviors were  
747 investigated for each concentration reached in the accumulated layers and revealed by *in-situ* SAXS  
748 experiments. The integration of the *in-situ* shear rate fields obtained from the velocity field by micro-  
749 PIV into the rheological laws gives access to the calculated *in-situ* stress field of the concentrated  
750 layers.

751 These measurements allowed revealing certain mechanisms of flow in link with the rheological  
752 behavior evolutions of the suspensions, induced by the simultaneous effect of velocity and pressure at  
753 the vicinity of the membrane surface during the filtration process. It thus was highlighted several  
754 specific flow regions with well-identified behaviors. Firstly, a region A has been identified at the  
755 nearest vicinity to the membrane surface, for which there is no velocity, corresponding to a suspension  
756 at rest. Secondly a region B for which the shear rate and corresponding calculated shear stress start to  
757 increase until reaching a maximum. In this region the shear flow forces are sufficiently high compare  
758 to colloidal interactions and pressure forces, to initiate the flow of the suspension. This region B can  
759 be assimilated as the concentration polarization layer. These two first regions A and B had a thickness  
760 of about a few hundreds of micrometer. Their thickness evolves according to the time of filtration and  
761 the operating conditions, the history of shear flow involved and the physico-chemical conditions of  
762 the suspensions. This original information has led to the stress level required to involve a flow  
763 between regions A and B during the filtration process and for different physico-chemical conditions of  
764 the suspensions, which highlights the important role played by the rheological behavior in the  
765 formation of the concentrated layers. Lastly, a third region C is defined in which the suspension  
766 reaches the conditions where the suspension is circulating in the feed channel without being affected  
767 by any concentration phenomenon. The concentration of the suspension is constant and corresponds to  
768 the initial filtered concentration, with a decreasing shear rate until reaching the maximum velocity  
769 value between 2000 and 2500  $\mu\text{m}$  above the membrane towards the center of the cell.

770 From a fundamental point of view, obtaining the stress levels inside the concentrated layers, related to  
771 the concentration profile, the cross-flow and the rheological behavior of the filtered suspensions,  
772 improves the understanding of the phenomena involved in the formation of the concentrated layers and  
773 fouling phenomena. From an industrial point of view, this work allows to improve the efficiency of  
774 ultrafiltration since it gives a better understanding of the formation of these phenomena.

775

## 776 **ACKNOWLEDGEMENTS**

777 We would like to thank Theyencheri Narayanan and Michael Sztucki (ESRF, Grenoble) for their kind  
778 help in scattering experiments and fruitful discussions, Jean-Jacques Lasserre (Dantec Dynamics) for  
779 his help and productive discussions, William Chèvremont for his helps in stress calculations.  
780 Mohamed Karrouch, Eric Faivre, H el ene Galliard, Didier Bl es es and Fr ed eric Hugenell (Laboratoire  
781 Rh eologie et Proc ed es, Grenoble) and Jacques Gorini (ESRF, Grenoble) for technical assistance. We  
782 gratefully acknowledge the ESRF for the SC 4177 beam time allocation. This work was supported by  
783 the Labex TEC 21 (Investissements d'Avenir - grant agreement n o ANR-11-LABX-0030). LRP and  
784 LGP2 are part of PolyNat Carnot Institut (Investissements d'Avenir - grant agreement no. ANR-11-  
785 CARN-030-01) and of program (ANR-15-IDEX-02).

## 786 **REFERENCES**

- 787 [1] C. Romero, R. Davis, Global-Model of Cross-Flow Microfiltration Based on Hydrodynamic  
788 Particle Diffusion, *J. Membr. Sci.* 39 (1988) 157–185.
- 789 [2] L. Song, M. Elimelech, Theory of concentration polarization in crossflow filtration, *J. Chem. Soc.*  
790 *Faraday Trans.* 91 (1995) 3389–3398.
- 791 [3] W.R. Bowen, P.M. Williams, Quantitative predictive modelling of ultrafiltration processes:  
792 Colloidal science approaches, *Surf. Forces Wetting Phenom. Membr. Sep. Rheol. Top. Issue*  
793 *Honour Victor Starov.* 134–135 (2007) 3–14.
- 794 [4] M. Elimelech et S. Bhattacharjee, A novel approach for modeling concentration polarization in  
795 crossflow membrane filtration based on the equivalence of osmotic pressure model and filtration  
796 theory, *J. Membr. Sci.* 145 (1998) 223-241.
- 797 [5] P. Bacchin, D. Si-Hassen, V. Starov, M. J. Clifton, et P. Aimar, A unifying model for  
798 concentration polarization, gel-layer formation and particle deposition in cross-flow membrane  
799 filtration of colloidal suspensions, *Chem. Eng. Sci.* 57 (2002) 77-91.
- 800 [6] Y. El Rayess, C. Albasi, P. Bacchin, P. Taillandier, M. Mietton-Peuchot, et A. Devatine, Analysis  
801 of membrane fouling during cross-flow microfiltration of wine, *Innov. Food Sci. Emerg. Technol.*  
802 16 (2012) 398-408.
- 803 [7] E. M. V. Hoek and M. Elimelech, Cake-Enhanced Concentration Polarization: A New Fouling  
804 Mechanism for Salt-Rejecting Membranes, *Environ. Sci. Technol.* 37(2003) 5581-5588.
- 805 [8] O.R. Lokare, S. Tavakkoli, S. Wadekar, V. Khanna, R. D. Vidic, Fouling in direct contact  
806 membrane distillation of produced water from unconventional gas extraction, *J. Membr. Sci.* 524  
807 (2017) 493–501.
- 808 [9] G. Gesan-Guiziou, R. J. Wakeman, et G. Daufin, Stability of latex crossflow filtration: cake  
809 properties and critical conditions of deposition, *Chem. Eng. J.* 85 (2002) 27-34.

- 810 [10] B. Espinasse, P. Bacchin, et P. Aimar, Filtration method characterizing the reversibility of  
811 colloidal fouling layers at a membrane surface: Analysis through critical flux and osmotic pressure  
812 , *J. Colloid Interface Sci* 320 (2008) 483-490.
- 813 [11] P. Bacchin, A. Marty, P. Duru, M. Meireles, et P. Aimar, Colloidal surface interactions and  
814 membrane fouling: Investigations at pore scale, *Adv. Colloid Interface Sci.* 164 (2011) 2-11.
- 815 [12] J. C. Chen, Q.Li, M.Elimelech, In situ monitoring techniques for concentration polarization and  
816 fouling phenomena in membrane filtration, *Adv. Colloid and Interface Sci.* 107 (2004) 83-108.
- 817 [13] Y. Marselina , Lifia, P. Le-Clech, R.M.Stuetz, V. Chen, Characterisation of membrane fouling  
818 deposition and removal by direct observation technique, *J. Membr. Sci.* 341 (2010) 163-171.
- 819 [14] X. Huang, G.R. Guillen, E.M.V. Hoek, A new high-pressure optical membrane module for direct  
820 observation of seawater RO membrane fouling and cleaning, *J. Membr. Sci.* 364 (2010) 149-156.
- 821 [15] S. Beaufort, S. Alfenore, C. Lafforgue, Use of fluorescent microorganisms to perform in vivo and  
822 in situ local characterization of microbial deposits, *J. Membr. Sci.* 369 (2011) 30-39.
- 823 [16] J. Fernández-Sempere, F. Ruiz-Beviá, R. Salcedo-Díaz, Measurements by holographic  
824 interferometry of concentration profiles in dead-end ultrafiltration of polyethylene glycol solutions,  
825 *J. Membr. Sci.* 229 (2004) 187-197.
- 826 [17] D. Airey, S. Yao, J. Wu, V. Chen, A.G. Fane, J.M. Pope, An investigation of concentration  
827 polarization phenomena in membrane filtration of colloidal silica suspensions by NMR micro-  
828 imaging, *J. Membr. Sci.* 145 (1998) 145-158.
- 829 [18] R.M. Mc Donogh, H. Bauser, N. Stroh, U .Grauschopf, Experimental in-situ measurement of  
830 concentration polarisation during ultra- and micro-filtration of bovine serum albumin and Dextran  
831 Blue solutions, *J. Membr. Sci.* 104 (1995) 51-63.
- 832 [19] J. Mendret, C. Guigui, P. Schmitz and C. Cabassud, Dead-end ultrafiltration and backwash:  
833 dynamic characterisation of cake properties at local scale, *Desalination* 199 (2006) 216-218.
- 834 [20] J. Mendret, C. Guigui, P. Schmitz and C. Cabassud and P. Duru, An optical method for in situ  
835 characterization of fouling during filtration, *AIChE J.* 53 (2007) 2265-2274.
- 836 [21] J. Mendret, C. Guigui, P. Schmitz and C. Cabassud, In situ dynamic characterisation of fouling  
837 under different pressure conditions during dead-end filtration: Compressibility properties of  
838 particle cakes, *J. Membr. Sci.* 333 (2009) 20-29.
- 839 [22] G.C. Agbangla, E. Climent, and P. Bacchin, Experimental investigation of pore clogging by  
840 microparticles: Evidence for a critical flux density of particle yielding arches and deposits,  
841 *Separation and Purification Technology* 101 (2012) 42-48.
- 842 [23] Z.Sendekie, and P. Bacchin, Colloidal Jamming Dynamics in Microchannel Bottlenecks,  
843 *Langmuir* 32 (2016) 1478-1488.
- 844 [24] S. Lorenzen, Y. Ye, V. Chen , M.L. Christensen, Direct observation of fouling phenomena during  
845 cross-flow filtration: Influence of particle surface charge, *J. Membr. Sci.* 510 (2016) 546-558.
- 846 [25] T. Mattsson, W.J.T. Lewis, Y.M.J. Chew, M.R. Bird, The use of fluid dynamic gauging in  
847 investigating the thickness and cohesive strength of cake fouling layers formed during cross-flow  
848 microfiltration, *Separation and Purification Technology* 198 (2018) 25-30.

- 849 [26] T. J. Su, J. R. Lu, Z. F. Cui, R. K. Thomas, R. K. Heenan, Application of Small Angle Neutron  
850 Scattering to the in Situ Study of Protein Fouling on Ceramic Membranes, *Langmuir* 14 (1998)  
851 5517-5520.
- 852 [27] D. Antelmi, B. Cabane, M. Meireles, P. Aimar, Cake Collapse in Pressure Filtration, *Langmuir* 17  
853 (2001) 7137-7144.
- 854 [28] J. B. Madeline, M. Meireles, C. Bourgerette, R. Botet, R. Schweins, B. Cabane, Restructuring of  
855 Colloidal Cakes during Dewatering, *Langmuir* 23 (2007) 1645-1658.
- 856 [29] F. Pignon, A. Magnin, J.M. Piau, B. Cabane, P. Aimar, M. Meireles and P. Lindner, Structural  
857 characterisation of deposits formed during frontal filtration, *J. Membr. Sci.* 174 (2000) 189-204.
- 858 [30] F. Pignon, A. Alemdar, A. Magnin and T. Narayanan, Small-Angle x-ray scattering studies of Fe-  
859 montmorillonite deposits during ultrafiltration in a magnetic field, *Langmuir* 19(21) (2003) 8638-  
860 8645 .
- 861 [31] F. Pignon, G. Belina, T. Narayanan, X. Paubel, A. Magnin and G. Gésan-Guiziou, Structure and  
862 rheological behavior of casein micelle suspensions during ultrafiltration process, *The Journal of*  
863 *Chemical Physics* 121 (2004) 8138-8146.
- 864 [32] C. David, F. Pignon, T. Narayanan, M. Sztucki, G. Gésan-Guiziou and A. Magnin, Spatial and  
865 temporal in situ evolution of the concentration profile during casein micelle ultrafiltration probed  
866 by small-angle x-ray scattering, *Langmuir* 24 (2008) 4523-4529.
- 867 [33] F. Pignon, M. Abyan, C. David, A. Magnin and M. Sztucki, In situ Characterization by SAXS of  
868 Concentration Polarization Layers during Cross-Flow Ultrafiltration of Laponite Dispersions,  
869 *Langmuir* 28 (2012) 1083-1094.
- 870 [34] Y. Jin, N. Hengl, S. Baup, F. Pignon, N. Gondrexon, A. Magnin, M. Sztucki, T. Narayanan, L.J.  
871 Michot and B. Cabane, Effects of ultrasound on colloidal organization at nanometer length scale  
872 during cross-flow ultrafiltration probed by in-situ SAXS, *J. Membr. Sci.* 453 (2014) 624-635.
- 873 [35] Y. Jin, N. Hengl, S. Baup, F. Pignon, N. Gondrexon, M. Sztucki, G. Gésan-Guiziou, A. Magnin,  
874 M. Abyan, M. Karrouch, D. Blésès, Effects of ultrasound on cross-flow ultrafiltration of skim milk:  
875 characterization from macro-scale to nano-scale, *J. Membr. Sci.* 470 (2014) 205-218.
- 876 [36] Y. Jin, N. Hengl, S. Baup, G. Maitrejean, F. Pignon, Modeling and analysis of concentration  
877 profiles obtained by in-situ SAXS during cross-flow ultrafiltration of colloids, *J. Membr. Sci.* 528  
878 (2017) 34-45.
- 879 [37] G. Cano, P. Steinle, J.V. Daurelle, Y. Wyart, K. Glucina, D. Bourdiol and P. Moulin,  
880 Determination of pressure and velocity fields in ultrafiltration membrane modules used in drinking  
881 water production, *J. Membr. Sci.* 431 (2013) 221-232.
- 882 [38] H. T. Kim, J. E. Cha, B. W. Rhee, H.-L. Choi, H. Seo, and I. C. Bang, Measurement of Velocity  
883 and Temperature Profiles in the 1/40 Scaled-Down CANDU-6 Moderator Tank, *Science and*  
884 *Technology of Nuclear Installations* (2015) 1-9.
- 885 [39] F. Arndt, U. Roth, and H. Nirschl, S. Schütz, G. Guthausen, New Insights into Sodium Alginate  
886 Fouling of Ceramic Hollow Fiber Membranes by NMR Imaging, *AIChE Journal* 62 (2016) 2459-  
887 2467.
- 888 [35] C. Martin, F. Pignon, A. Magnin, J.M. Piau, P. Lindner and B. Cabane, Dissociation of  
889 thixotropic clay gels, *Phy. Rev. E* 66 (2002) 021401.

- 890 [36] F. Pignon, A. Magnin, J.M. Piau, B. Cabane, P. Lindner and O. Diat., A yield stress thixotropic  
891 clay suspension: investigations of structure by light, neutron and x-ray scattering, *Phys. Rev. E* 56  
892 (1997) 3281-3289.
- 893 [37] B. Ruzicka, L. Zulianb, E. Zaccarelli, R. Angelini, M. Sztucki, A.Moussaïd, and G. Ruocco,  
894 Competing Interactions in Arrested States of Colloidal Clays, *Phys. Rev. Lett.* 104 (2010) 085701.
- 895 [38] M. Pilavtepe, S. M. Recktenwald, R. Schuhmann; K. Emmerich and N. Willenbacher, Macro- and  
896 microscale structure formation and aging in different arrested states, *J. Rheol.* 62 (2018) 593-605.

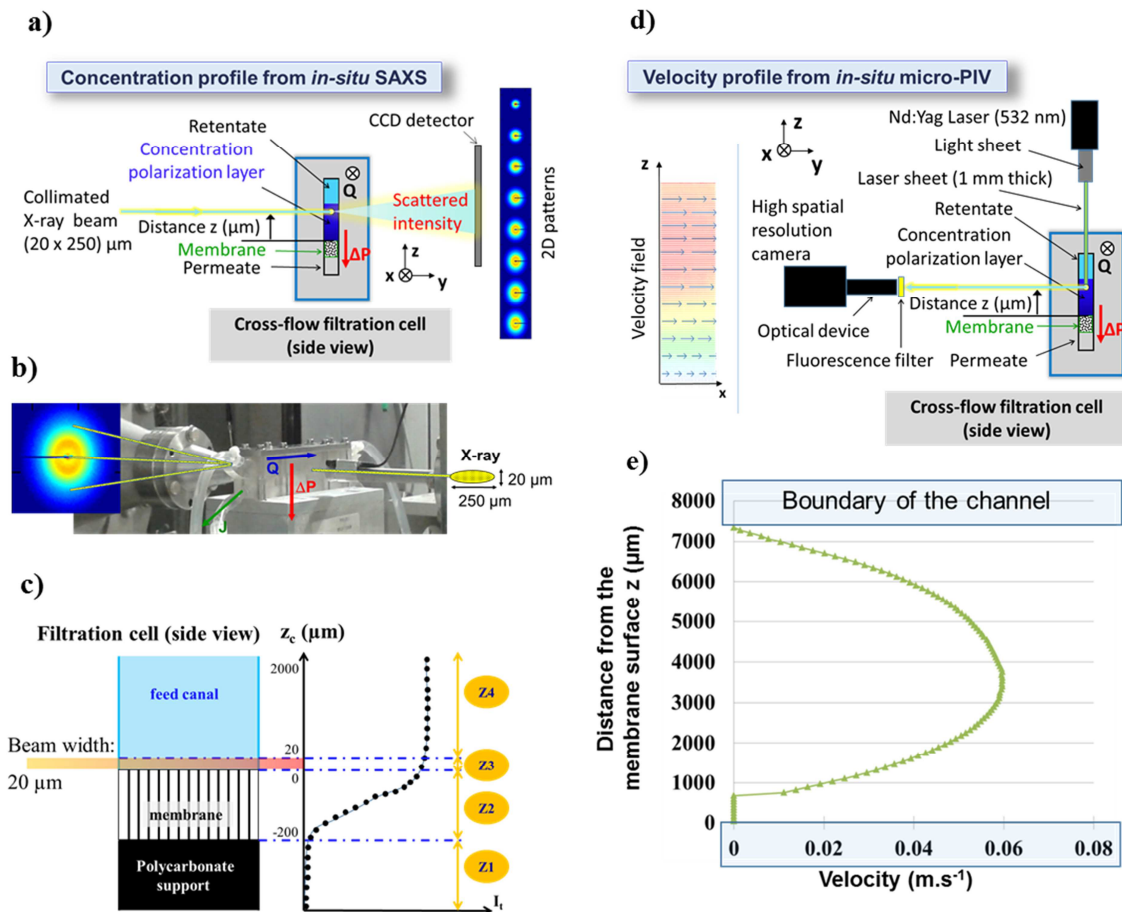
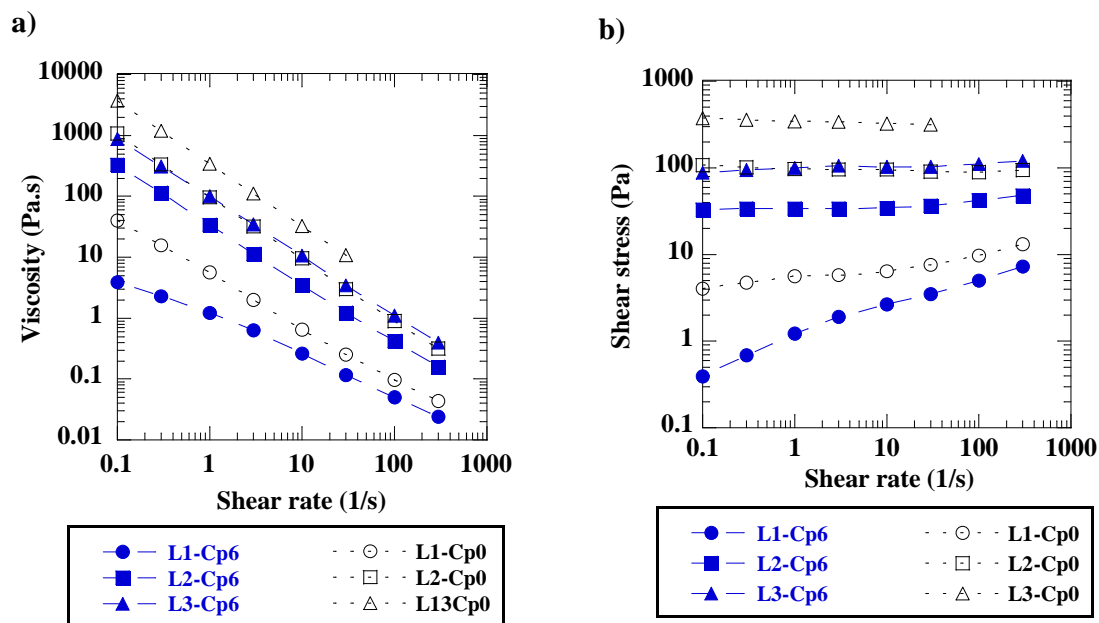


Fig. 1: Scheme of the *in-situ* a) b) and c) SAXS and d) micro-PIV measurements under cross-flow ultrafiltration process e) example of velocity profile inside the whole filtration channel for a laponite suspensions with peptizer, L1-Cp6,  $t_p = 12$  days,  $Q = 0.06 \text{ L}\cdot\text{min}^{-1}$ ,  $\text{TMP} = 1.1 \times 10^5 \text{ Pa}$ ,  $T = 25 \text{ }^\circ\text{C}$ .

901  
902  
903  
904  
905



906  
907  
908  
909  
910  
911

**Fig. 2:** Steady-state flow curves of Laponite dispersions ( $10^{-3}$  M NaCl, pH = 10) at different volume fractions and different peptizer concentrations.  $T = 25 \pm 1$  °C,  $t_p = 12$  days. a) viscosity and b) corresponding shear stress as a function of the imposed shear rate.

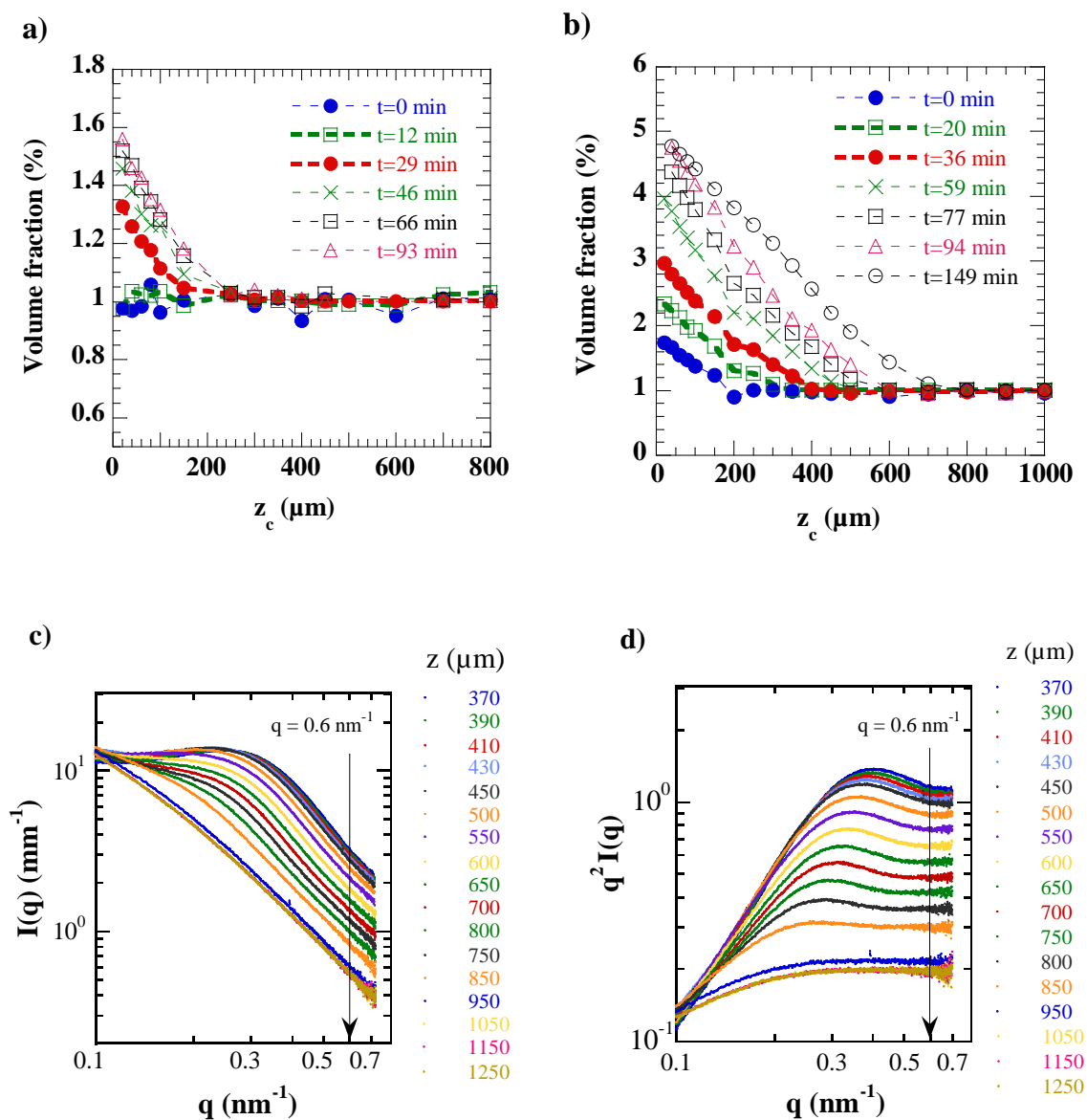


Fig. 3: Concentration profiles (volume fraction as a function of  $z_c$ ) deduced from *in-situ* SAXS measurements in the middle window: during the cross-flow ultrafiltration of Laponite suspensions with 6% tspp,  $t_p = 12$  days,  $\text{TMP} = 1.1 \times 10^5$  Pa,  $T = 25 \pm 1$  °C  
a) step 1  $Q = 0.3 \text{ L}\cdot\text{min}^{-1}$ , b) step 2  $Q = 0.06 \text{ L}\cdot\text{min}^{-1}$ , c) corresponding scattering intensities  $I(q)$  of the concentration profile (volume fraction as function  $z = z_c + 350 \mu\text{m}$ ) at  $t = 94$  min, 6% tspp and d) kratky plot representation ( $q^2 I(q)$ ) of the scattering intensity (same profile).

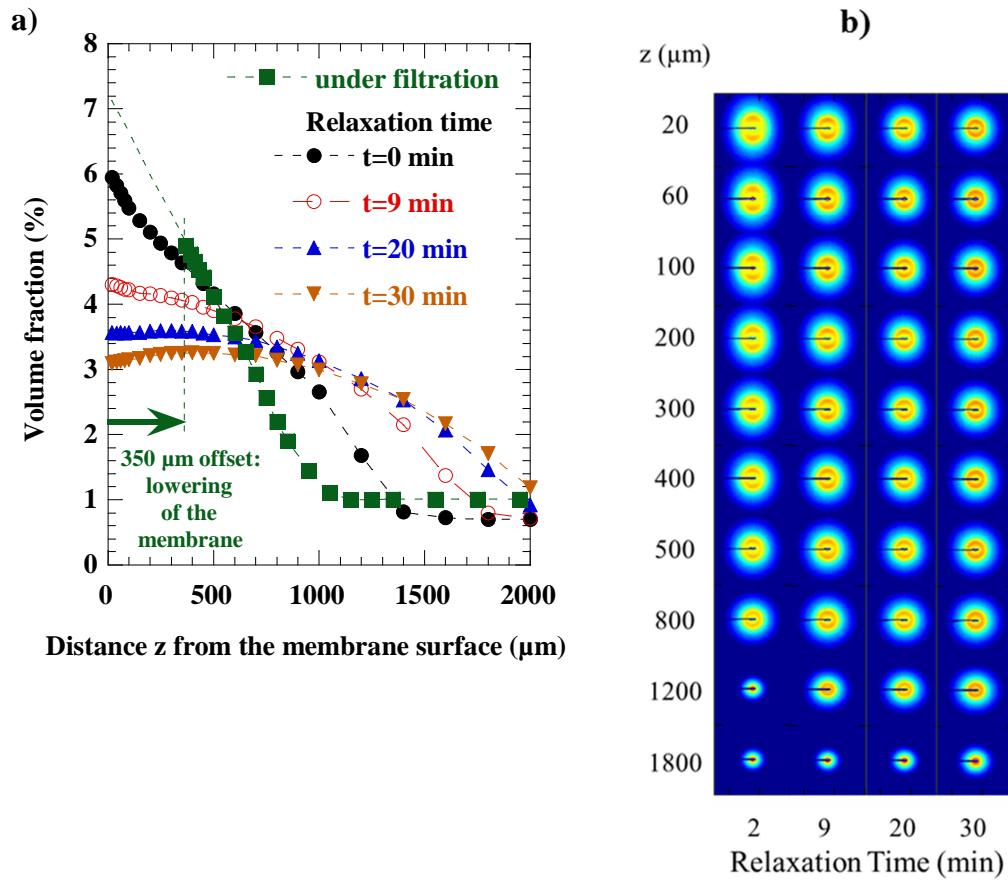


Fig. 4: a) Concentration profiles deduced from *in-situ* SAXS in the middle window during relaxation step (TMP = 0, Q = 0) of Laponite suspensions with 6% tspp, and b) corresponding 2D-SAXS patterns during relaxation. Sample distance = 2 m,  $t_p$  = 12 days,  $T = 25 \pm 1$  °C.

915

916

917

918

919  
920

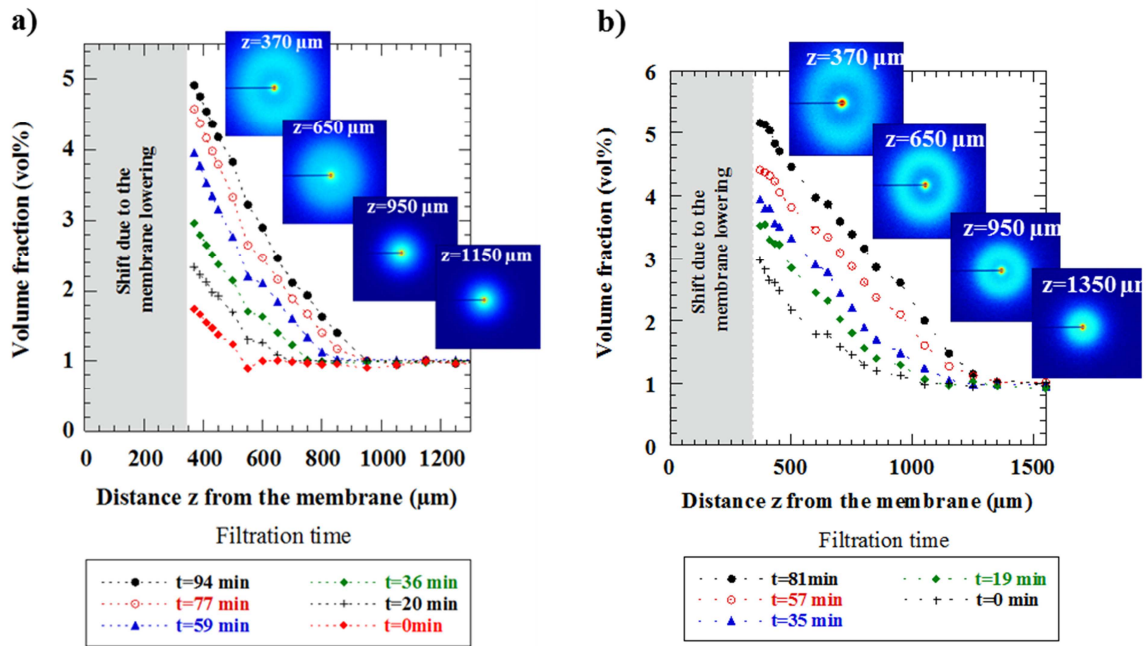
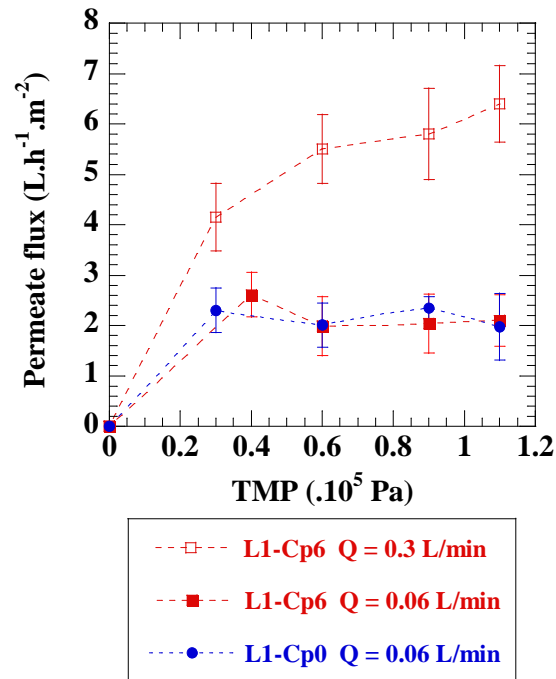


Fig. 5: Concentration profiles and SAXS pattern obtained by *in-situ* SAXS measurements in the middle window during the ultrafiltration process with lowering correction of a) Laponite suspensions with tspp (L1-Cp6) and b) Laponite suspensions without tspp (L1-Cp0). x position is the middle of the channel,  $Q = 0.06 \text{ L}\cdot\text{min}^{-1}$ ,  $t_p = 12 \text{ days}$ ,  $\text{TMP} = 1.1 \times 10^5 \text{ Pa}$ ,  $T = 25 \pm 1 \text{ }^\circ\text{C}$ .

921  
922  
923

924  
925  
926  
927



928  
929  
930  
931  
932  
933  
934

Fig. 6: Steady states J permeation flux as a function of transmembrane pressure conditions for different cross-flows measured during ultrafiltration of Laponite suspensions,  $t_p = 12$  days,  $T = 25 \pm 1$  °C.

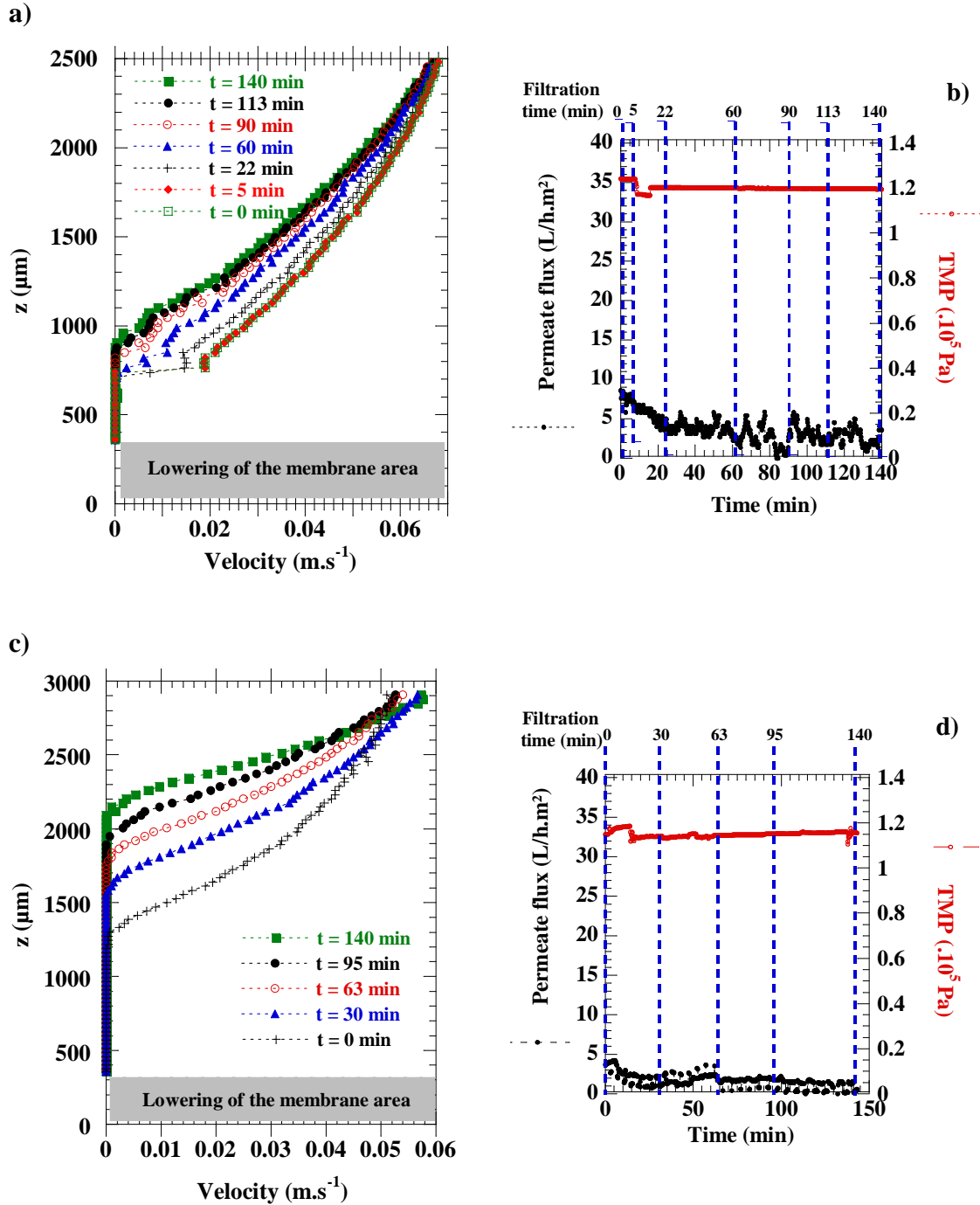


Fig. 7: Velocity profiles in the middle window and associated permeate flux for a Laponite suspension as a function of the distance  $z$  from the membrane surface (with lowering correction) during cross-flow ultrafiltration. a) and b) with peptizer (L1-Cp6), c) and d) without peptizer (L1-Cp0).  $x$  position is the middle of the channel,  $t_p = 12$  days,  $Q = 0.06 \text{ L}\cdot\text{min}^{-1}$ ,  $\text{TMP} = 1.1 \times 10^5 \text{ Pa}$ ,  $T = 25 \pm 1 \text{ }^\circ\text{C}$ .

936  
937  
938

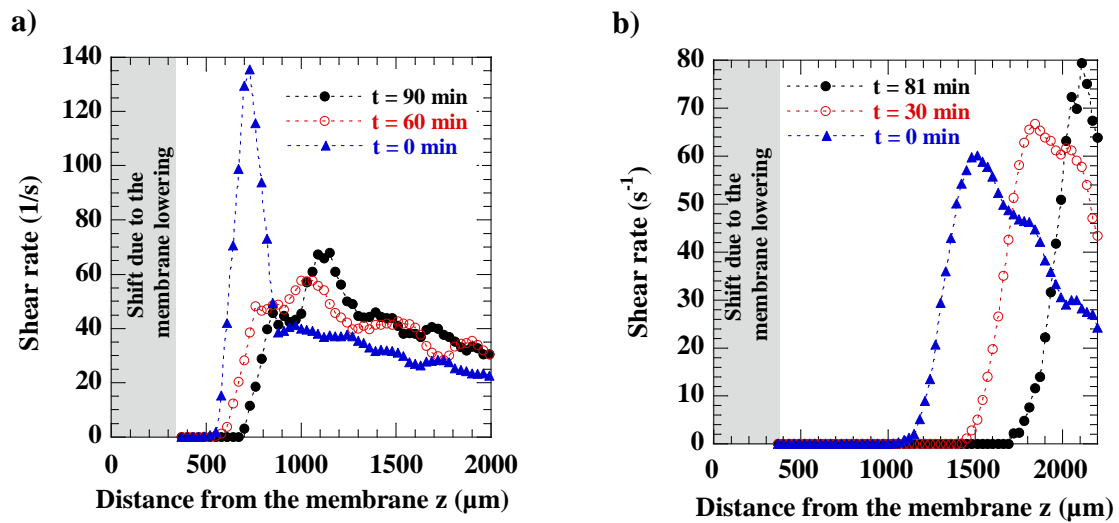


Fig. 8: Shear rates profiles in the concentrated layer formed during cross-flow ultrafiltration process as a function of the distance  $z$  from the membrane surface (with the lowering correction) during the last step of filtration. a) Laponite with peptizer (L1-Cp6), b) Laponite without peptizer (L1-Cp0).  $Q = 0.06 \text{ L}\cdot\text{min}^{-1}$ ,  $t_p = 12 \text{ days}$ ,  $\text{TMP} = 1.1 \times 10^5 \text{ Pa}$ ,  $T = 25 \pm 1 \text{ }^\circ\text{C}$ , middle window.

939  
940

941  
942  
943

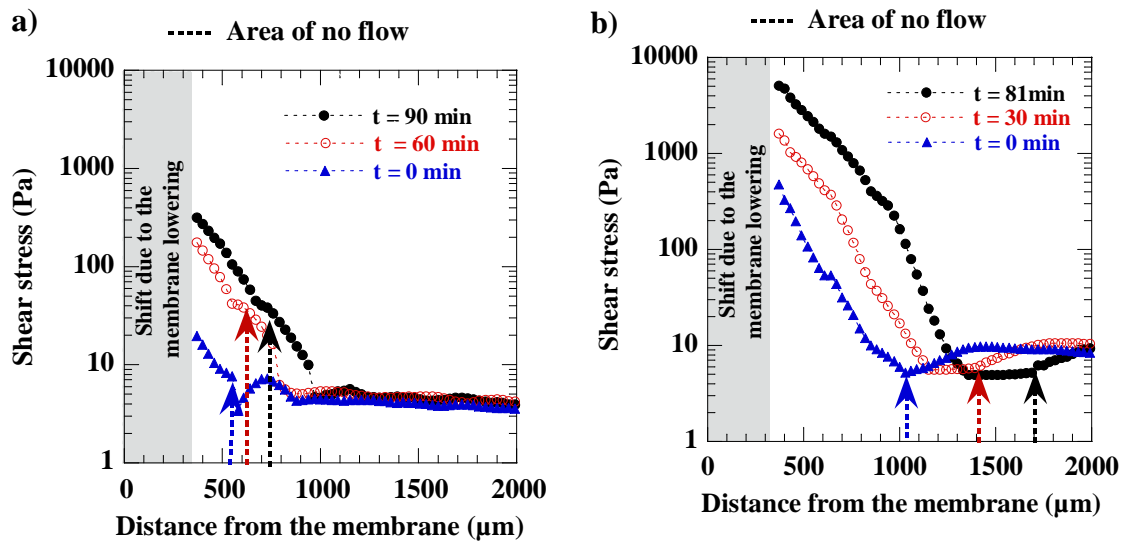


Fig 9: Shear stress profiles in the concentrated layer formed as a function of the distance  $z$  from the membrane surface (with the lowering correction) during the time of filtration. a) Laponite with peptizer (L1-Cp6), b) Laponite without peptizer (L1-Cp0).  $Q = 0.06 \text{ L}\cdot\text{min}^{-1}$ ,  $t_p = 12 \text{ days}$ ,  $\text{TMP} = 1.1 \times 10^5 \text{ Pa}$ ,  $T = 25 \pm 1 \text{ }^\circ\text{C}$ , middle window.

944  
945

946  
947  
948

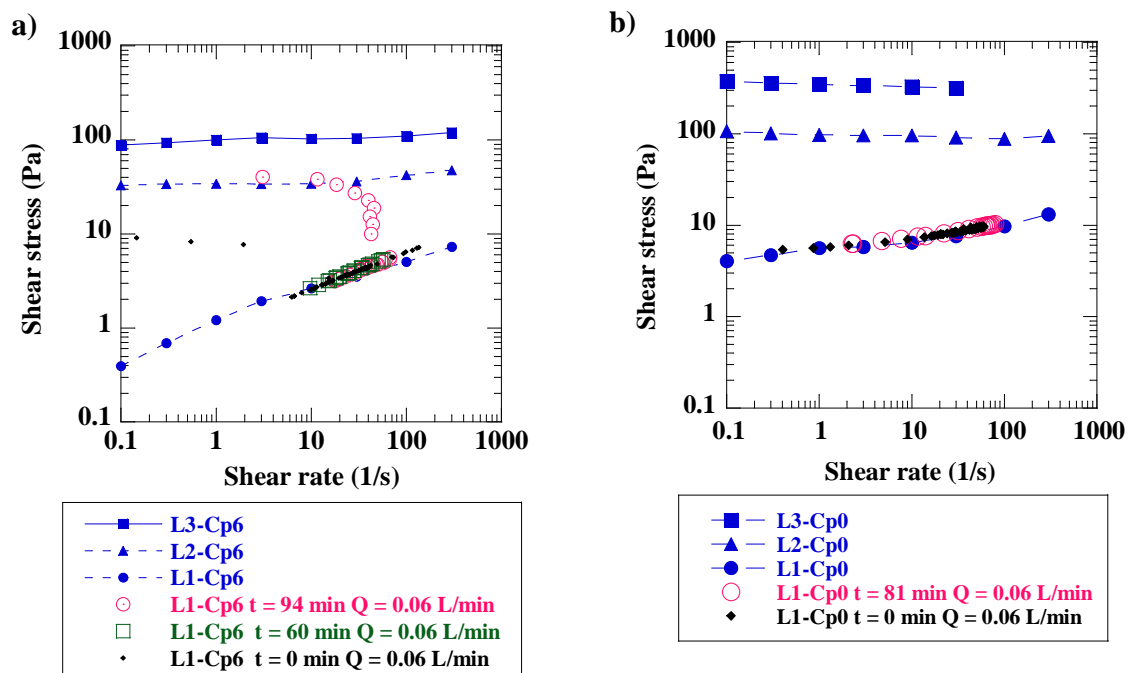


Fig 10: Rheological behavior obtained by rheometric measurements and with shear stresses calculated in the concentration polarization layer deduced from SAXS and micro-PIV experiments. a) Laponite with peptizer (L1-Cp6), b) Laponite without peptizer (L1-Cp0).  $t_p = 12$  days,  $T = 25 \pm 1$  °C.

949  
950

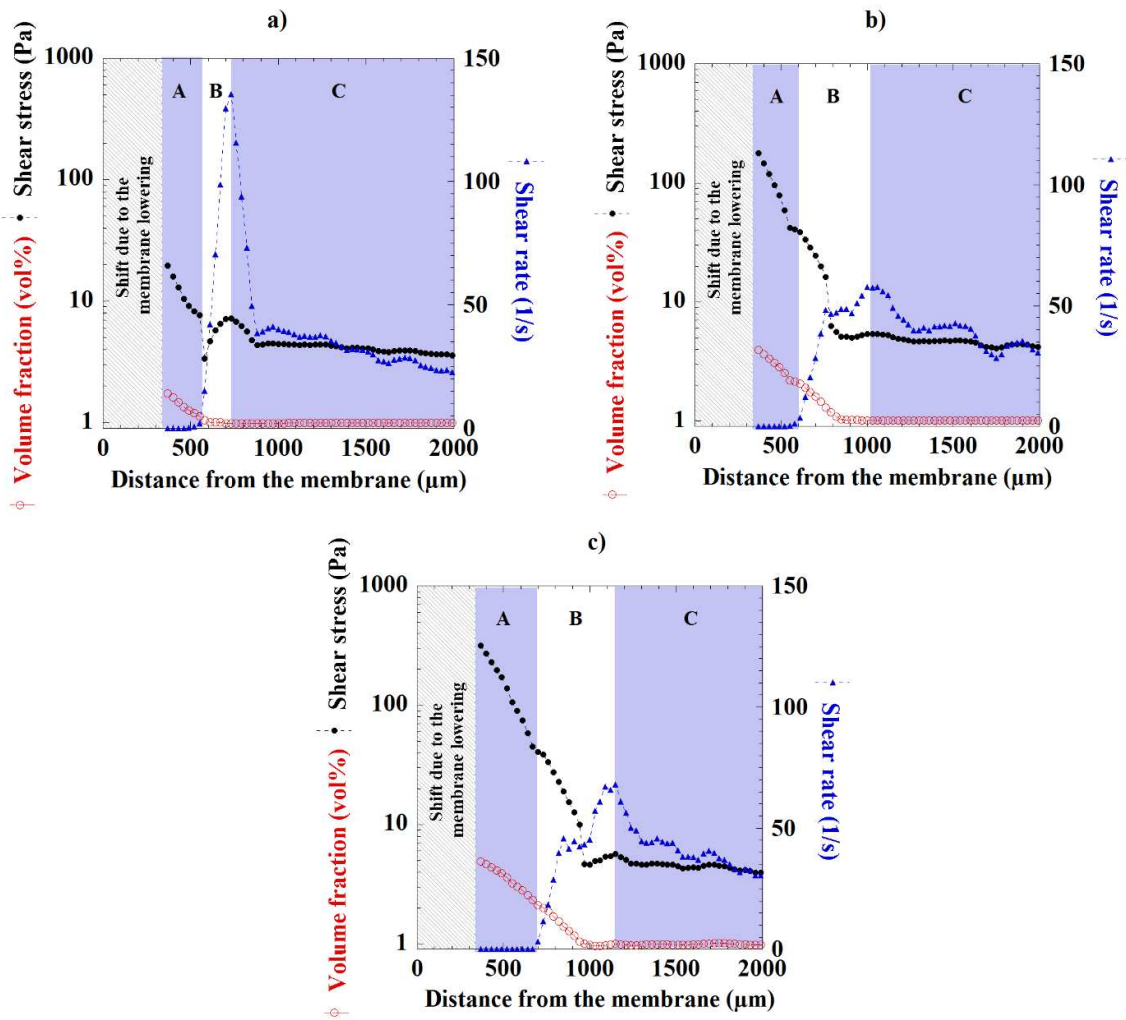


Fig. 11: Behavior regions A, B and C in the concentrated layer formed from Laponite suspensions with peptizer as a function of the distance  $z$  from the membrane surface (with the lowering correction) during cross-flow ultrafiltration, for the last step of filtration, Step 2,  $Q = 0.06 \text{ L}\cdot\text{min}^{-1}$ . At filtration time a)  $t = 0 \text{ min}$ , b)  $t = 60 \text{ min}$ , c)  $t = 90 \text{ min}$ . L1-Cp6,  $t_p = 12 \text{ days}$ ,  $\text{TMP} = 1.1 \times 10^5 \text{ Pa}$ ,  $T = 25 \pm 1 \text{ }^\circ\text{C}$ , middle window.

951

952

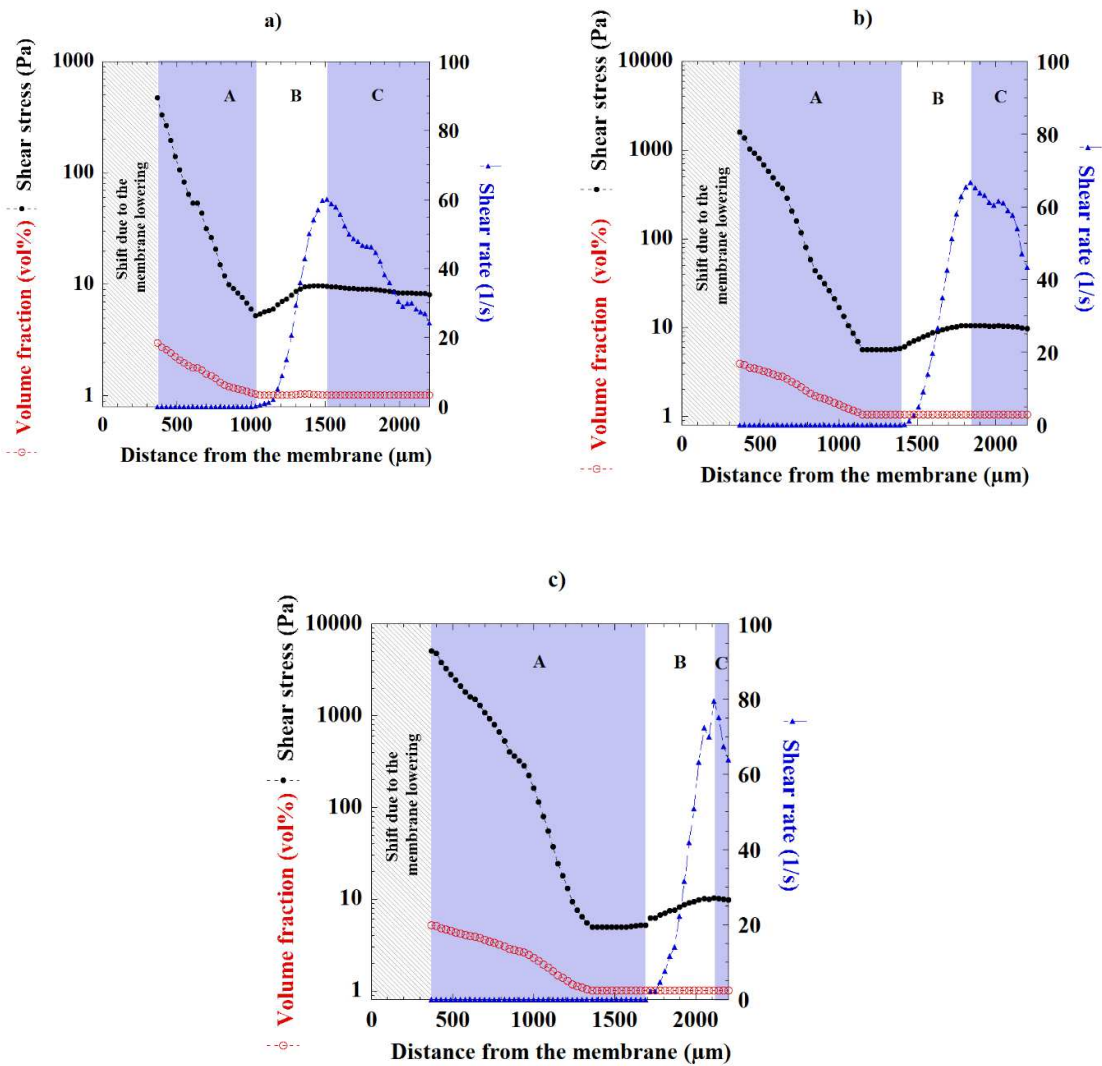


Fig. 12: Behavior regions A, B and C in the concentrated layer formed from Laponite suspensions without peptizer as a function of the distance  $z$  from the membrane surface (with the lowering correction) during cross-flow ultrafiltration, for the last step of filtration, Step 3,  $Q = 0.06 \text{ L}\cdot\text{min}^{-1}$ . At filtration time a)  $t = 0$  min, b)  $t = 35$  min, c)  $t = 81$  min. L1-Cp0,  $t_p = 12$  days,  $\text{TMP} = 1.1 \times 10^5 \text{ Pa}$ ,  $T = 25 \pm 1 \text{ }^\circ\text{C}$ .

956

Suspension	Flow rate (L.min <sup>-1</sup> )	Transmembrane pressure (x 10 <sup>5</sup> Pa)	Time (min)	N° of filtration step
L1-Cp6	0.3	1.1	80	1
	0.06	1.1	149	2
	0	0	30	3
L1-Cp0	0.3	1.1	70	1
	0.2	1.1	57	2
	0.06	1.1	141	3

957

958

959 *Table 1: description of the filtration procedure for suspensions of Laponite with peptizer (L1-*  
960 *Cp6) and without peptizer (L1-Cp0).*

961

